metals

MDPI

Article

Post Neutron Irradiation Recovery and Recrystallization of ITER Grade Forged Tungsten Bar

Dimitrios Papadakis [1,2,*], Efthimios Manios [1] and Konstantina Mergia [1]

[1] Institute of Nuclear and Radiological Sciences and Technology, Energy and Safety, NCSR "Demokritos", 15310 Athens, Greece; ef.manios@ipta.demokritos.gr (E.M.); kmergia@ipta.demokritos.gr (K.M.)
[2] Department of Physics, School of Sciences, University of Athens, 15772 Athens, Greece
* Correspondence: d.papadakis@ipta.demokritos.gr

Abstract: Defect recovery and recrystallization studies of neutron-irradiated tungsten (W) addressing the microstructural evolution in relation to the mechanical properties, provide valuable insight into defect interactions and annihilation processes. Understanding these mechanisms can aid in the development of effective healing processes, potentially extending the lifespan of fusion reactor components. Additionally, this research helps to elucidate how neutron exposure alters the behaviour of materials used in fusion reactor components, contributing to improved design and durability. Within this framework, an ITER grade forged W bar was neutron irradiated to a damage of 0.21 displacements per atom at 600 °C and subsequently isochronally annealed from 700 up to 1550 °C in 50 °C steps. Irradiation causes the formation of dislocation loops and vacancy clusters as well as the formation of Re and Os transmutation products, leading to a 35% increase in hardness and a 23% increase in resistivity. The evolution of the microstructure after isochronal annealing is investigated through positron annihilation lifetime spectroscopy, X-ray diffraction, resistivity, and Vickers hardness measurements. The total dislocation line density as well as the number density and size of voids are determined as a function of annealing temperature. Specifically, the critical resolved stresses of dislocations and voids are correlated with their densities and distinct recovery stages are identified. The kinetics of defect annihilation are discussed in relation to the annealing temperature. Nearly complete dislocation annihilation occurs after annealing at 1300 °C, followed by complete void dissolution and recrystallization at 1450 °C.

Keywords: neutron-irradiated tungsten; recovery; recrystallization; positron annihilation lifetime spectroscopy; electrical resistivity; hardness

Academic Editor: Arne Mattias Thuvander

Received: 21 December 2024
Revised: 31 January 2025
Accepted: 6 February 2025
Published: date

Citation: Papadakis, D.; Manios, E.; Mergia, K. Post Neutron Irradiation Recovery and Recrystallization of ITER Grade Forged Tungsten Bar. *Metals* **2025**, *15*, x. https://doi.org/10.3390/xxxxx

1. Introduction

The development of fusion as a sustainable energy source requires the overcoming of significant technological challenges, particularly in selecting viable materials and achieving efficient plasma confinement. To withstand the extreme heat loads, encountered in the fusion environment, and damaging particles produced in Deuterium–Tritium fusion reaction, the plasma-facing components (PFCs) will be armored with tungsten (W), with both the divertor and first wall in ITER comprised of W components [1]. W offers numerous advantages including low tritium retention and the highest melting temperature of any natural element. Additionally, it exhibits very good thermo-physical properties, such as good sputtering resistance, low swelling, thermal stress

and shock resistance, and high-temperature strength [2–7]. It suffers, however, from high ductile-to-brittle transition temperature (DBTT), low fracture toughness, and low recrystallization temperature, especially when compared to the expected temperatures in a fusion device. These factors impose limitations on its performance under operational conditions. To address these challenges, several microstructural modifications have been proposed [4], with cold rolling [8,9] and forging [10] being among the most promising approaches [4,10,11] compared to other W grade options.

Plasma-facing components will be exposed to high temperatures (above 600 °C), high heat loads [12], and intense neutron irradiation. Neutron irradiation causes atomic displacements resulting in the creation of vacancy clusters or voids and dislocation loops [13–18] as well as transmutation, namely rhenium (Re), osmium (Os), and tantalum (Ta), as well as hydrogen and helium [19]. These transmuted elements can form precipitates [20] or solid solution clouds around voids, loops, and precipitates enriched with Re and Os [21,22]. These defects will cause material hardening and embrittlement and will eventually limit the component lifetime beyond the design limits. To emulate the fusion neutron irradiation damage on W, fission neutron irradiation at high temperatures [13,15,17–19,21–28] or ion irradiation [29–33] are employed. The specific neutron irradiation conditions, such as the irradiation temperature, neutron spectrum, and damage rate and dose define the type and population of generated defects [20,23,24,26–28,34].

Besides the neutron damage in magnetically confined plasma fusion devices, interaction with the plasma, especially during disruptions, can cause local temperature spikes in plasma-facing materials, further altering their microstructure and thus their properties. From a technological perspective, it is crucial to prevent recrystallization of the material in order to retain ductility and avoid crack formation during operation, even though avoiding recrystallization after disruption events is highly unlikely [35]. Therefore, studying the microstructural evolution of neutron-irradiated polycrystalline tungsten after annealing is crucial for two main reasons: firstly, to elucidate the recovery stages [36,37], and secondly, to assess the recrystallization resistance of neutron-irradiated material. This will aid in the development of tailored annealing processes aiming at extending the lifetime of fusion reactor components.

Regarding the recovery of neutron- or ion-irradiated tungsten, the main findings of numerous investigations are outlined as follows: In the range of 400 to 600 °C, stage III recovery occurs entailing monovacancy migration [17,31,38–43]. Above 650 °C and up to 900 °C, stage IV recovery takes place, involving the coalescence of small vacancy clusters [17,37,39,41–44], as well as the growth of dislocation loops and the rearrangement of the dislocation line [17,31,39,40,44,45]. The evolution of interstitial-type dislocation loops, which are the predominant types of dislocation loops in neutron-irradiated tungsten, arises from loop–vacancy interactions such as vacancy-mediated climb. This occurs either through pipe diffusion at low temperatures or bulk diffusion at higher temperatures. Additionally, loop–loop interactions, such as self-climb, contribute to the coalescence of loops [46]. Especially in high-temperature and dose irradiation, the annealing of loops occurs from the absorption of equilibrium vacancies since the density of available unbound vacancies in the lattice is extremely low [46]. Further annealing results in complete defect recovery, which has been observed at the temperatures of 900 °C [41], 1300 °C [17], 1500 °C [37,42,47], and 1700 °C [48] depending on the irradiation conditions.

Regarding recrystallization, it is important to address a common misconception about the term “recrystallization temperature”. In reality, a single recrystallization temperature does not exist, as recrystallization is an energy-driven process. This means that increasing the annealing time lowers the recrystallization temperature and vice versa [49]. A more accurate, quantitative method for comparing recrystallization resistance involves using activation energy or temperature-dependent time to halve recrystalliza-

tion [50–56]. It is essential to recognize that the energy required for recrystallization depends on microstructural factors such as grain size, cold/hot working, and impurities. As a result, recrystallization in tungsten can occur over a broad temperature range, from 1100 °C for 1 h [57] up to 1500 °C for 30 min [54], with various intermediate temperatures and times [55,56,58–70].

In this study, an ITER grade forged W bar, neutron irradiated to 0.21 displacements per atom (dpa) at 600 °C, was isochronally annealed from 700 to 1550 °C for 24 h in 50 °C steps, along with two non-irradiated counterparts. The evolving microstructure was investigated through X-ray diffraction (XRD), positron annihilation lifetime spectroscopy (PALS), electrical resistivity, and Vickers hardness. The recovery of the neutron damage, along with the correlation between microstructure, hardness, and resistivity, is discussed. The total dislocation line density as well as the number density and size of voids were determined as a function of the annealing temperature. Specifically, the critical resolved stresses of dislocations and voids were correlated with their densities and individual recovery stages were identified, discussing the kinetics of defect annihilation versus annealing temperature. The current research builds on and complements our previous study regarding the microstructural evolution of post neutron irradiation annealed tungsten [37,71].

2. Materials and Methods

2.1. Material, Neutron Irradiation, and Post-Irradiation Annealing

The tungsten (W) material, provided by PLANSEE SE (Reutte, Austria), was fabricated in bar form with a purity exceeding 99.97% using a powder metallurgy approach. This process involved sintering, followed by hot forging from two orthogonal directions, and a final stress-relief annealing at 1000 °C for 1 h [66,72]. Disks, each 1 mm thick, were cut with their surface normal perpendicular to the bar's axis using electrical discharge machining. These disks were then mechanically polished on both sides with diamond suspension, with a final polishing step of colloidal silica. The final sample thickness was approximately 0.5 mm. The manufacturer specifications for the maximum and typical impurity levels [73] are presented in Table 1.

Table 1. Impurity contents of W in bar produced by Plansee SE.

Impurities	**Ag**	**Al**	**As**	**Ba**	**Ca**	**Cd**	**Co**	**Cr**	**Cu**	**Fe**	**K**	**Mg**	**Mn**	**Na**	**Nb**
Guaranteed [μg/g]	10	15	5	5	5	5	10	20	10	30	10	5	5	10	10
Typical [μg/g]	<5	5	<2	<2	<2	<2	<2	<5	<5	10	5	<2	<2	<2	<5
Impurities	**Ni**	**Pb**	**Ta**	**Ti**	**Zn**	**Zr**	**Mo**	**C**	**H**	**N**	**O**	**P**	**S**	**Si**	
Guaranteed [μg/g]	5	5	20	5	5	5	100	30	5	5	20	20	5	20	
Typical [μg/g]	<2	<2	<10	<2	<2	<2	20	10	2	<2	5	<10	<2	5	

The samples were irradiated in the BR2 reactor (for which the typical spectra can be found in [74]), at SCK CEN at 600 °C for a duration of 70 days to a neutron fluence of about 8.9×10^{20} n/cm^2, for E > 0.1 MeV. This fast neutron fluence corresponds to a dose of 0.21 dpa, as determined by MCNPX 2.7.0 [75] calculations using a threshold displacement energy of 55 eV, according to IAEA recommendations [76]. The fission neutron spectrum of the BR2 reactor [74] is considered as adequately representative of the one expected to be encountered in the DEMO divertor [77], highlighting the importance of the experimental data presented and their relevance to fusion material research. The irradiation temperature of 600 °C is characteristic of the steady state regime at a 10 MW/m^2 power load for the ITER and DEMO divertors [24]. The dose of 0.21 dpa is both ITER relevant and representative of the early-stage material changes during DEMO reactor

operation, considering that for the divertor tungsten armor, the expected dose rate is 3 dpa/fpy [78]. The irradiation temperature was determined within a 5% uncertainty, based on thermo-hydraulic calculations. The estimated temperature fluctuations, caused by the neutron flux fluctuations and the burn out of the fuel element within a reactor cycle, were approximately 25 K. The samples were encapsulated in a stainless steel tube filled with helium. The thickness of the steel tube was 1.5 mm and it was selected to maximize the shielding from the thermal neutrons and minimize, therefore, the transmutation production. More details about the irradiation can be found in [79]. The transmutation products of Re, Os, and Ta were determined using the FISPACT-II nuclide inventory code [80], employing the TENDL-2019 nuclear library for Re and Os, and the EAF-2010 library for Ta. The results showed (0.54 ± 0.06) at% Re, (0.013 ± 0.002) at% Os, and (3.3 ± 0.4) × 10^{-3} at% Ta. It is noted that EAF-2010 was used for the evaluation of the W transmutation into Ta, as it provides a better agreement between the experimental specific activities, determined via gamma spectroscopy, and the calculated values using the EAF-2010 nuclear library.

Both irradiated and non-irradiated samples were annealed under high vacuum (~10^{-6} mbar) from 700 to 1550 °C in 50 °C steps for an interval of 24 h at each temperature.

The following terminology is used to distinguish between the various sample conditions: (a) *non-irradiated sample* refers to the material state before any irradiation and heat treatment, (b) *as-irradiated sample* refers to the state after irradiation to 0.21 dpa at 600 °C, but before any annealing, (c) *post-irradiation annealed (PIA) sample* refers to the irradiated sample after annealing at a specific temperature (it is noted that the annealing at different temperatures was performed on the same sample), and (d) *control sample* denotes the non-irradiated sample annealed under the same conditions as the PIA sample.

Since the irradiated samples had not been electropolished, the control samples were kept with the same surface condition. However, whenever necessary, the property/parameter in consideration of a non-irradiated electropolished sample is provided to facilitate the discussion of the results.

2.2. X-Ray Diffraction (XRD) and Grazing Incidence X-Ray Diffraction (GIXRD)

The crystalline structure was investigated by X-ray diffraction (XRD) measurements carried out at room temperature using a Bruker AXS (Karlsruhe, Germany) D8 diffractometer equipped with a Cu K_α X-ray source, a Göbbel mirror to produce a parallel beam, a scintillator detector, a soller collimator between the sample and the detector, and proper optical slits after the Göbbel mirror to define the angular resolution. A LaB_6 660c NIST standard [81] was measured to determine the instrumental resolution near the (110) reflection of W (2θ = 40.26 degrees) and was found to be (0.090 ± 0.002) degrees. To increase the sensitivity to secondary phase detection, Grazing Incidence XRD (GIXRD) measurements were carried out at an incidence angle of 1.0 degree.

2.3. Scanning Electron Microscopy (SEM)

The grain structure was probed using a Thermo Fisher Scientific™ Apreo™ 2 scanning electron microscope (Eindhoven, Netherlands). The images were acquired using a backscatter detector, on an accelerating voltage of 30 kV, a spot size of 14, and a working distance of 5 mm.

2.4. Positron Annihilation Lifetime Spectroscopy (PALS)

Positron Annihilation Lifetime Spectroscopy measurements were carried out at room temperature, using the Ortec® PLS-system (Oak Ridge, TN, USA). A ^{22}Na positron source was used, encapsulated in 7.5 mg/cm² thin polyimide (Kapton®) windows. More details on the experimental setup can be found in [82]. The LT10 software (v. 10.2.2.2)

[83,84] was used to analyse the PALS data. This is performed by fitting the following equation to the experimental data:

$$S(t) = B + R(t) \otimes (I_{src} + I_s) = B + R(t) \otimes \left(\sum_{k=1}^{L} I_k \lambda_k e^{-\lambda_k t} + \sum_{i=0}^{N} I_i \lambda_i e^{-\lambda_i t} \right) \quad (1)$$

The above expression comprises a sum of exponential components representing contributions from the source, I_{src}, and the sample, I_s, convoluted with the resolution function $R(t)$, which is assumed Gaussian, and superimposed on the background B. $i = 0$ refers to the defect-free material, and $i = 1,...,N$ to the various open volume defects of the sample. I_i and $\tau_i = 1/\lambda_i$ characterize the intensity and lifetime of each component, respectively. The components k account for contributions from air, Kapton®, and the source in the spectrum. To determine the source parameters, a set of well-annealed reference materials (Al, Ni, Cd, and Pb) with high purity (≥99.99%) was analyzed. The source part of the spectrum comprises annihilations in the ^{22}Na source and Kapton® foil (since their lifetimes are nearly identical) and annihilations in the air contained between the source and the specimen. The analysis above assumes that positron annihilations occur independently within each defect and the defect-free matrix, with no interactions or correlations between them.

From the analysis of the data, the lifetime, τ_i, of each type i of defect and the intensity, I_i, of the positron to be annihilated in type i defect ($\sum I_i = 1$) are determined.

2.5. DC Electrical Resistivity

Electrical resistance was measured using the collinear 4-point probe (4PP) method. To this end, a Keithley 2182A nanovoltmeter and Keithley 6221 AC and DC **(Cleveland, OH, USA)** source were employed. The current used was in the range 1–100 mA and the probe spacing, i.e., the distance between every two probes, was s = 1.5875 mm. The measurements were carried out in "Delta Mode", synchronizing the current source and nanovoltmeter, eliminating the thermoelectric voltage contribution in the measurements. The measured resistance is converted to resistivity through a geometric factor, $F = \frac{\rho}{R}$, dependent on the sample's dimensions and shape [82]. The geometric factor consists of the product of two different factors referring to the finite thickness of the sample, F_1, and to the lateral width diameter of the disk-shaped sample, F_2, assuming that the probes are placed in the center of the sample [85]. The final geometric factor expression is:

$$F = F_1 \cdot F_2 = \frac{\pi s}{\int_0^\infty \coth(\mu t/s)\{J_0(\mu) - J_0(2\mu)\} d\mu} \cdot \frac{\ln(2)}{\ln(2) + \ln\left[\frac{(d/s)^2 + 3}{(d/s)^2 - 3}\right]} \quad (2)$$

where s is the probe spacing, t and d the sample's thickness and diameter, respectively, and J_0 is the Bessel function of the first kind of order zero. All the resistivity measurements were carried out at 19 °C.

2.6. Hardness

Vickers indentation experiments were performed at a maximum load of 3 N using a NANOVEA's mechanical tester. Preliminary indentation tests were performed to determine the dwell time of 200 s at maximum load and the (un)loading rate of 20 N/min for which stability in the hardness values and minimal creep are achieved. Each measure-

ment comprised six indentation tests, spaced by 200 μm. The Vickers hardness, H_V, was determined employing the equation:

$$H_V = \frac{F_{\max}}{A_C} = \frac{2F_{\max}}{d_{mean}^2}\sin(\alpha/2) \quad (3)$$

where A_C is the contact area of the indenter, determined from optical microscopy images of the residual imprint after the indentation tests, $F_{\max}$ is the maximum applied force, d_{mean} is the mean diagonal length measured from corner to corner on the residual impression in the specimen surface, and $a = 136°$ is the face angle of the square-based diamond pyramid of the Vickers indenter.

3. Experimental Results

The discussion of the experimental results after annealing is correlated with the observed microstructure and properties of the non-irradiated and the as-irradiated samples. All reported errors refer to the standard error of the mean, unless otherwise stated.

3.1. Grain Structure

The non-irradiated tungsten forged bar's microstructure consists of grains with an average grain size of 16 μm and elongated subgrains along the bar axis, with sizes in the range of 2.3–4 μm and 0.6–1.7 μm along and perpendicular to the bar axis, respectively [24]. The average dislocation density is about 4.5×10^{12} m^{-2} with very few (density below 10^{20} m^{-3}) but large (>50 nm) dislocation loops present [24].

SEM images of the non-irradiated and as-irradiated materials are presented in Figure 1.

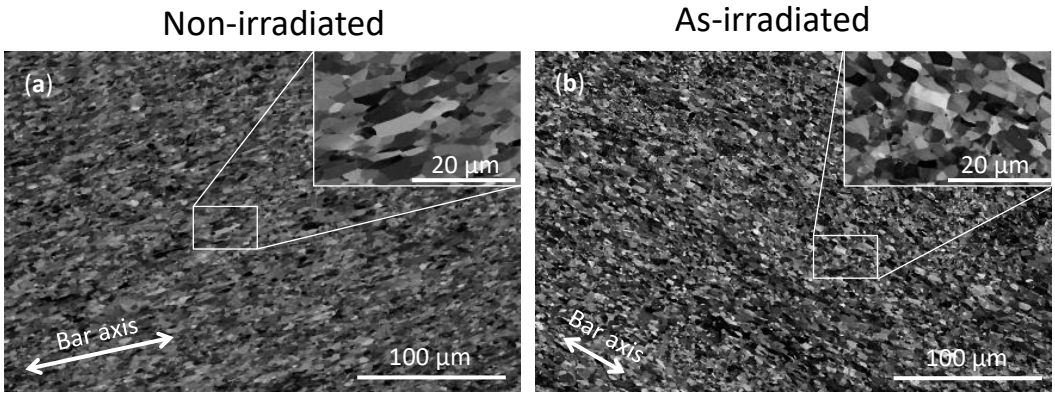

Figure 1. SEM images of the non-irradiated (**a**) and as-irradiated (**b**) W bars. The bar axis direction is shown.

An analysis regarding the subgrain size is made as detailed in the ASTM standard E112-12 [86]. The specific procedure used is the planimetric one by which each grain is counted separately. The reported grain size corresponds to the diameter of the grain considered as equiaxial. This allows for the determination of the relative frequency of the appearance of different sizes of grains, and the possible analysis using a distribution. The most common distribution for grain sizes is the log-normal distribution [87]:

$$D = \frac{A}{\sqrt{2\pi}\cdot\sigma\cdot x}\exp\left(-\frac{\left(\ln x-\mu^{*}\right)^{2}}{2\sigma^{*2}}\right) \quad (4)$$

where μ^{*} and σ^{*} are the mean and standard deviation of the subgrain size's natural logarithm, respectively, and A is a normalization parameter.

The subgrain size distributions analysis from the SEM investigation is presented in Figure 2, with the determined log-normal distribution parameters in Table 2.

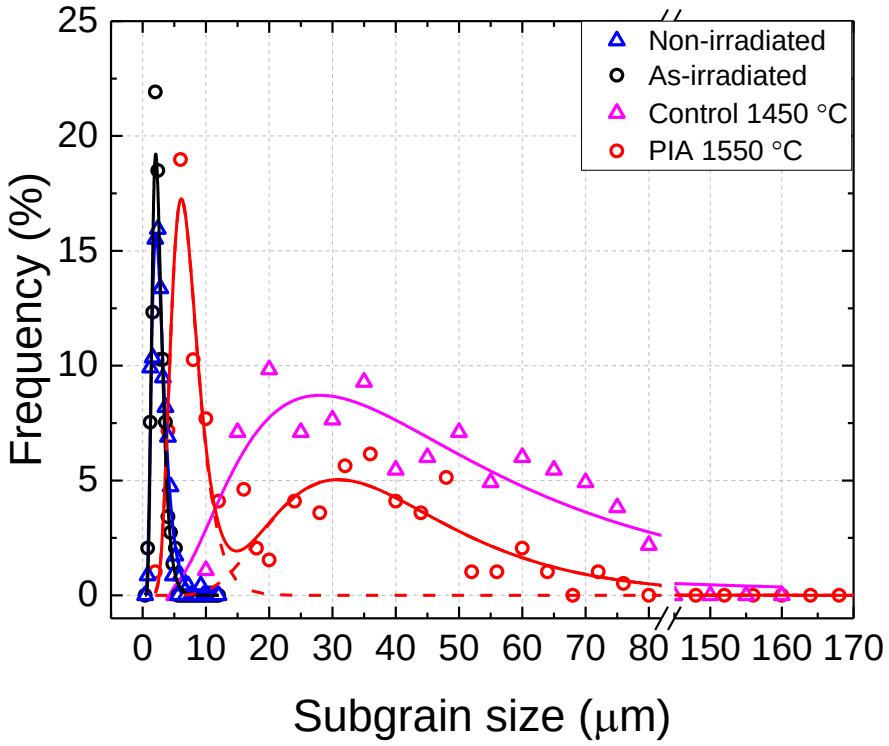

Figure 2. Subgrain size distributions of the non-irradiated (△), as-irradiated (○), control annealed at 1450 °C (△), and post-irradiation annealed (PIA) at 1550 °C (○) W bar samples from SEM investigation. Solid lines: see text and Table 2. The dashed red lines for the PIA at 1550 °C sample correspond to the two log-normal distributions that make up the observed distribution.

Table 2. Determined subgrain sizes of the W bar materials derived from the log-normal distributions presented in Figure 2.

Sample		Mean Subgrain Size, μ (μm)	Standard Deviation, σ (μm)
Non-irradiated		2.85 ± 0.06	1.35 ± 0.04
As-irradiated		2.54 ± 0.05	0.97 ± 0.03
Control—1450 °C		46 ± 1	25.0 ± 0.7
PIA—1550 °C	Fine grain distrib.	7.3 ± 0.2	2.6 ± 0.1
	Coarse grain distrib.	41 ± 2	20 ± 2

The determined mean grain sizes prior to annealing are in accordance with the subgrain sizes determined by TEM [24], with the grain structure remaining unaffected by the irradiation.

After irradiation, the microstructure is characterized predominantly by dislocation loops and voids, with relatively few dislocation lines. The dislocation loops are heterogeneously distributed within the grains, in the form of rafts or individual loops, having

an average density of (2.3 ± 0.8) × 10^{22} m^{-3} and an average diameter of (2.8 ± 1.6) nm corresponding to a line density of (2.2 ± 1.2) × 10^{14} m^{-2} [24]. Dislocation lines, with a density approximately 10 times lower than the dislocation line density that corresponds to loops, are also present. Voids, which are randomly distributed within the matrix, have a density of (4.1 ± 1.1) × 10^{22} m^{-3} and an average diameter of (1.4 ± 0.3) nm.

For the PIA bar, after annealing at 1550 °C, abnormal grain growth, i.e., the pronounced growth of grains in a particular crystallographic direction relative to others, is observed. This is evident from the double log-normal peak shown in Figure 2 with parameters presented in Table 2. The microstructure exhibits a wide distribution of grain sizes, with some grains reaching up to 100 μm in diameter, while smaller subgrains, approximately ~2 μm in size, remain detectable. This abnormal grain growth suggests that grain growth has not been completed yet for the irradiated bar after PIA at 1550 °C, indicating an increased recrystallization resistance resulting from the prior neutron irradiation.

SEM images showing significant grain growth are presented in Figure 3, with the control sample annealed at 1450 °C and the irradiated sample after PIA at 1550 °C.

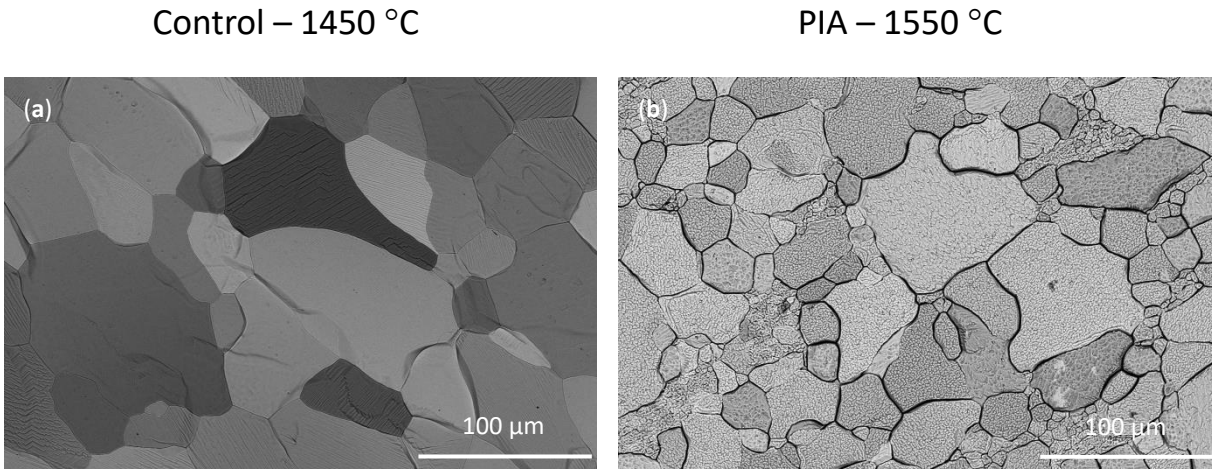

Figure 3. SEM images after annealing at 1450 °C of the control (**a**) and after post-irradiation annealing at 1550 °C of the irradiated (**b**) W bar.

3.2. Open Volume Defect Evolution Versus Annealing

PALS measurements were carried out after each step of isochronal annealing on both the control and the irradiated samples. The results are depicted in Figure 4 for the annealed control samples and in Figure 5 for the PIA samples. The measured positron lifetimes are linked to specific open volume defects, particularly vacancies, vacancy clusters, and dislocations. From the evolution of the determined positron lifetimes, the evolution of these defects is inferred.

The PALS spectrum of the non-irradiated mechanically polished sample exhibits a positron lifetime of (153 ± 1) ps, equal, within error bar, to that of the electropolished non-irradiated sample (152 ± 1) ps, as can be observed in Figure 4. This lifetime originates mainly from positron annihilations in dislocations present in the material due to the forging process. In the literature, the reported positron lifetime for dislocations lies in the range from 130 to 180 ps, whereas the positron lifetime for the defect-free tungsten is reported in the range of 100–116 ps ([79] and references therein). The determined lifetime may include a small contribution of vacancies which present a lifetime in the range (160–200 ps) ([79] and references therein) as will be discussed below.

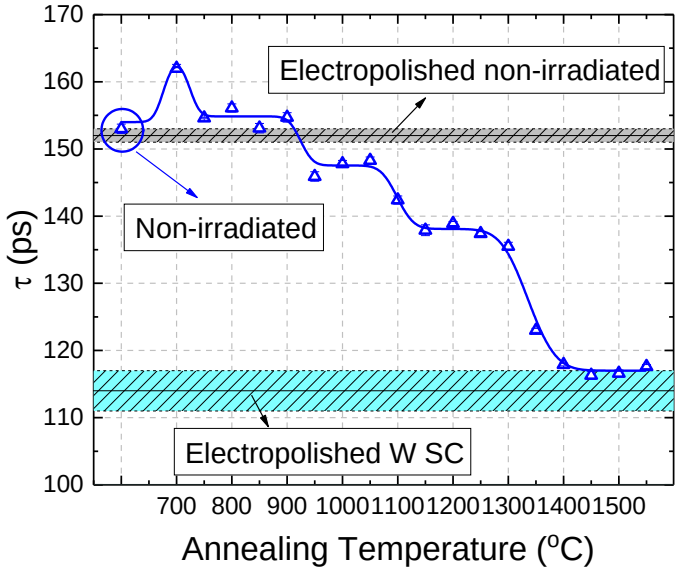

Figure 4. Positron lifetime after each step of isochronal annealing for the control sample. The positron lifetime of the electropolished W sample and the electropolished pristine W(100) single crystal (SC) [37] are also shown for reference. Solid line: guide to the eye. Adapted from [71].

For the control sample, a single positron lifetime component was needed to describe the PALS spectra after each annealing step (Figure 4). This lifetime, however, is an effective lifetime, containing information about all the abovementioned annihilation mechanisms of the positron.

A small increase in the lifetime to the value of (162 ± 1) ps is observed after annealing at 700 °C. This increase may be related to the emission of vacancies bound at dislocations or impurities [88], which would raise the effective positron lifetime. It has been shown that vacancies associated with dislocations [89,90] and vacancy impurity element complexes [91–94] are shallower positron traps than free vacancies in the bulk of the material, exhibiting shorter positron lifetimes. Therefore, the de-trapping of vacancies after annealing at 700 °C could explain the observed increase in the apparent lifetime, which then decreases as these vacancies are annealed out at 750 °C. After annealing in the range from 950 to 1050 °C, the positron lifetime decreases to about 147 ps and continues to decrease with further annealing reaching 123 ps after annealing at 1350 °C. This reduction suggests enhanced dislocation annihilation at this temperature. After annealing at 1450 °C, complete recovery of the defects (mainly dislocations) resulting from the forging process [95] occurs, as evidenced by the positron lifetime reaching 116 ps, which corresponds to that of the defect-free material.

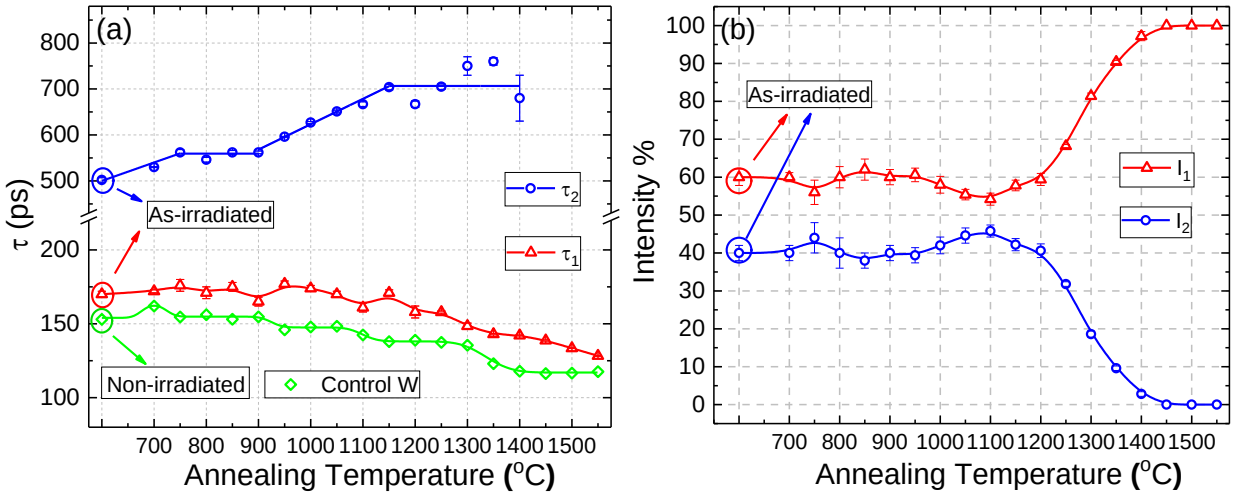

Figure 5. Positron lifetimes, τ_1 (△) and τ_2 (○) (**a**), and their relative intensities I_1 (△) and I_2 (○) (**b**), as determined by PALS, after each step of post-irradiation isochronal annealing for the irradiated W sample. The solid lines are guides to the eye. The lifetime of the control sample is also shown for reference. Adapted from [71].

For the irradiated sample, two positron lifetimes were required to describe the PALS spectra, a short, τ_1, and a long, τ_2, lifetime. The short lifetime, τ_1, represents a weighted average of lifetimes of positrons being annihilated in the defect-free bulk (100–116 ps), in dislocations (130–180 ps), and in mono-vacancies (160–200 ps) ([79] and references therein). The long lifetime, τ_2, is associated with positron annihilations in vacancy clusters or voids with a diameter larger than 1 nm, corresponding to a vacancy cluster containing more than 40 vacancies. For such void sizes, theoretical calculations suggest that the positron lifetime exhibits minimal or no dependence on void size due to positron localization at the void surface, reaching a saturation lifetime of approximately 500 ps [96,97].

Up to PIA at 1150 °C, τ_1 remains almost constant, while a continuous decrease is observed up to annealing at 1550 °C. Since τ_1 is a weighted average, this decrease, corresponding to a reduction in the contribution of positron annihilations in dislocations in the lifetime component, indicates dislocation annihilation.

The increase in the value of τ_2 after specific steps of PIA corresponds to an increase in the average size of vacancy clusters, which occurs in two stages: Directly after PIA up to 750 °C, and after annealing in the range of 950–1150 °C. As will be discussed afterwards, the first step can be attributed to de-trapping of vacancies and their subsequent coalescence. The second stage suggests an Ostwald ripening process [98], where larger clusters grow at the expense of smaller ones, driven by the decrease in the total surface free energy. Positron lifetimes exceeding 500 ps have been attributed to pick-off annihilations of ortho-positronium within large vacancy clusters [17,42], indicating partial decoration of the internal surface of these clusters by impurities [17]. Therefore, the positron lifetime values observed for the voids in the current study may also be related to the segregation of Re/Os at the void surface, as evidenced by other experiments at a higher irradiation dose [22,99].

The relative intensities of the positron lifetime components can provide additional information regarding the evolving microstructure. The relative intensity, I, is proportional to the trapping rate, κ, of the defect. The positron trapping rate is equal to the

defect number density, N_{def}, multiplied by the trapping strength, μ, of the defect [100], i.e., $I \propto \kappa = \mu \cdot N_{def}$. An increase in the relative intensity of the long lifetime, I_2, such as that after PI annealing from 950 to 1100 °C, could either indicate a decrease in the dislocation density or an increase in the trapping strength of the voids with increasing void size. The vacancy cluster positron trapping rate, however, has been shown to increase almost linearly with the number of vacancies in the cluster [101], and the increase is expected to slow down as the number of vacancies increases [102]. Thus, the increase in void size with the accompanied decrease in void density, even in the case of perfect conservation of vacancies, cannot be attributed to an increase in the trapping rate of voids. Therefore, the increase in the relative intensity of the long lifetime, I_2, is solely attributed to the reduction in the dislocation density. The reduction in relative intensity at temperatures above 1250 °C can be attributed to void dissolution (Figure 5b). Complete void dissolution is observed following PIA at 1450 °C.

3.3. DC Electrical Resistivity

DC electrical resistivity measurements at room temperature were performed after each step of isochronal annealing on both the irradiated and the control samples. The determined resistivity after each step of isochronal annealing is presented in Figure 6 for both the control and irradiated samples. For the non-irradiated reference sample, the value presented is the average from a population of eight reference samples.

Regarding the control samples, a single regime of recovery can be observed in the range of 1250 to 1400 °C, which could be due to both dislocation annihilation but also recrystallization. Electron scattering from grain boundaries can influence the resistivity of polycrystalline materials [103] but is expected to decrease after grain growth has occurred. The resistivity value of the fully recovered and recrystallized sample after annealing at 1500 °C is close but does not coincide with that of the pristine W (100) SC, a fact that is attributed to a higher level of impurities present in the W bar (Table 1) compared to a pristine single crystal.

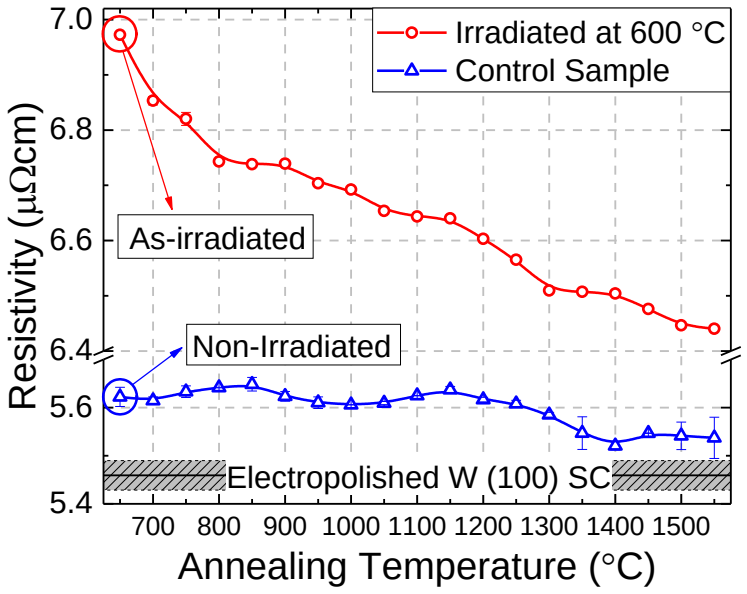

Figure 6. DC electrical resistivity after each step of post-irradiation annealing of the irradiated W bar sample. The resistivity of a pristine W(100) single crystal (SC) is provided for comparison. Solid lines: guides to the eye.

After irradiation, resistivity increases from (5.62 ± 0.02) μΩ·cm to (6.973 ± 0.001) μΩ·cm, an increase of ~24%, due to the creation of radiation-induced defects. An initial reduction in the resistivity after PIA up to 700 °C can be observed which continues with almost the same rate up to 800 °C. This reduction can be attributed to both dislocation annihilation, since dislocations are the primary contributors in radiation-induced resistivity, and vacancy de-trapping, as implied from the PALS results. Additionally, vacancy migration and clustering, as inferred from the hardness results in Section 3.5, likely contribute to this effect. Vacancies and small vacancy clusters contribute heavily to the measured resistivity; however, when large vacancy clusters or voids are formed, this contribution diminishes. For instance, for the same total number of vacancies, if they are arranged in vacancy clusters consisting of 10 vacancies, the contribution to resistivity is halved compared to the configuration of purely mono-vacancies. Two recovery mechanisms can be identified after PIA from 900 to 1150 °C and from 1150 to 1300 °C, both attributed to dislocation recovery. For higher annealing temperatures up to 1400 °C, the resistivity remains nearly constant, followed by a decrease after PIA at 1450 °C. This drop may be attributed to recrystallization and grain growth, as will be argued below.

The effect of grain boundaries on resistivity, ρ_{GB}, can be quantified using the Andrews method [104]:

$$\rho_{GB}(d) = \frac{A}{d} \tag{5}$$

where A is the Andrews parameter equal to 0.24 for W [105] and d the mean grain size.

The contribution of the subgrain size to the resistivity in the as-irradiated sample (subgrain size of 2.54 μm) and after PIA at 1500 °C (subgrain size of 22 μm) is determined to be ρ_{GB-irr} = 0.094 μΩ·cm and $\rho_{GB-1550°C}$ = 0.01 μΩ·cm (negligible), respectively. Taking into account that the grain size has not changed significantly after PIA up to 1400 °C, since recrystallization has not yet occurred, it follows that $\rho_{GB-irr} = \rho_{GB-1400°C}$ = 0.094 μΩ·cm, which is very close to the observed resistivity difference between PIA at 1550 °C and 1400 °C (~0.06 μΩ·cm). This supports the speculation that the decrease in resistivity between PIA at 1400 and 1550 °C is primarily due to grain growth.

To analyse the recovery processes involved in resistivity, using the Matthiessen's rule [106], the radiation-induced resistivity, RIR, which is the difference between the resistivity of the irradiated sample, ρ_{irr}, and that of the non-irradiated, ρ_{unirr} = (5.62 ± 0.02) μΩ·cm, can be expressed as [95]:

$$RIR \equiv \rho_{irr} - \rho_{unirr} = RIR_{void} + RIR_{disl} + RIR_{trans} \tag{6}$$

where RIR_{void}, RIR_{disl}, and RIR_{trans} are the contributions of voids, dislocations (both loops and lines), and transmutation products to the radiation-induced resistivity, respectively. It has been assumed that the grain boundaries contribute the same before and after irradiation, which is a valid assumption as has been discussed in Section 3.1. It has been demonstrated in the literature that texture also affects the resistivity of irradiated W materials [47], influencing both the type and number of radiation-induced defects, as well as their impact on resistivity depending on the preferential orientation within the crystal. For the purpose of this study, texture effects in resistivity are negligible since the texture as a function of the PIA temperature does not change significantly prior to grain growth as reported in [71].

RIR_{void} can be estimated [82], taking into account vacancy self-shielding in a cluster configuration [107–109], using the void diameter and number density as determined by

TEM in [36] and the specific resistivity of vacancies in tungsten ($P_{1V} \approx 10^{-34} \Omega \cdot m^4$) [110]. This contribution is estimated to be in the order of 10^{-2} μΩ·cm, and can, therefore, be considered negligible.

After PIA at 1550 °C, as indicated by PALS, XRD, and Vickers hardness results (the latter two to be discussed in Sections 3.4 and 3.5, respectively), tungsten has undergone complete recrystallization and is nearly defect free apart from the transmutation impurities. Consequently, RIR_{trans} can be directly determined by the following equation:

$$\rho_{PIA-1550°C} = \rho_{RX} + RIR_{trans} \quad (7)$$

where $\rho_{PIA-1550°C}$ = (6.440 ± 0.002) μΩ·cm and ρ_{RX} = (5.54 ± 0.04) μΩ·cm are the resistivities of the irradiated and control samples after annealing at 1550 °C, respectively. Thus, the resistivity contribution from transmutation products is determined to be RIR_{trans} = (0.90 ± 0.04) μΩ·cm. This is in satisfactory agreement with the calculated value of RIR_{trans} = (0.77 ± 0.08) μΩ·cm derived from the Re and Os concentrations obtained from neutronic calculations (Section 2.1), as well as the specific resistivity for rhenium P_{Re} (~1.3 μΩ·cm/Re at.%) [111] and for osmium P_{Os} (~5 μΩ·cm/Os at.%) [112], assuming that Re and Os are homogeneously distributed in the W matrix in solute form.

From the above, it can be inferred that the sole contributor to the increase in RIR up to 1300 °C is dislocations. The contribution of dislocations to RIR can be expressed using the following equation:

$$RIR_{disl} = P_{DSR} \cdot N_{disl} \quad (8)$$

where N_{disl} is the dislocation density and P_{DSR} the dislocation specific resistivity, which was determined as $P_{DSR} = 1 \times 10^{-23}\ \Omega \cdot m^3$ in our previous work [36].

From the experimentally determined resistivity and using Equations (6)–(8), the total dislocation density after each PIA step was determined and is presented in Figure 7. The TEM-determined dislocation density in [113] is included for comparison.

The dislocation density ((4.6 ± 0.9) × 10^{14} m^{-2}) in the as-irradiated state as determined from the resistivity is two times larger compared to the TEM-determined one ((2.2 ± 1.2) × 10^{14} m^{-2}). This discrepancy is attributed to the underestimation of the dislocation density from TEM, owing to the TEM's inability to resolve defects smaller than 1 nm, as discussed in [36]. The disagreement at the annealing temperatures of 800 and 1000 °C is mainly due to the annealing time difference between [36] and the present study, as well as the large uncertainties in determining the total dislocation line density from TEM when the dislocation loops have a wide size distribution.

The discrete regimes of dislocation recovery allowed for the splitting of the recovery into three separate stages. The initial decrease in dislocation density after annealing at 700 °C indicates a dislocation loop growth mechanism. The recovery stage from 900 to 1150 °C is associated with dislocation loop growth as well. The presence of two dislocation recovery regimes associated with dislocation loop growth could indicate the existence of areas with different dislocation loop densities. This could result in different interaction rates, with lower temperature loop growth occurring in the high-density region. Finally, the recovery from 1150 to 1300 °C is attributed to dislocation loop annihilation.

In addition to the microstructural information provided by resistivity, by itself, resistivity is proven to be a helpful engineering tool with regards to characterizing material properties of irradiated materials relevant to the operation of a fusion reactor. The electrical resistivity and the electronic contribution to the thermal conductivity, κ_e, are related through the Wiedemann–Franz law as $\rho \cdot \kappa_e = L \cdot T$ [114], where L is the Lorenz

number and T the temperature. Theoretically, if the free electrons are the sole contributors of thermal conductivity, the Lorenz number attains the Sommerfeld value of $L_0 = \frac{\pi^2 k^2}{3e^2}$ = 2.445 × 10^{-8} W·Ω·K^{-2}, where k is the Boltzmann constant and e the electron's charge. In tungsten, however, the Lorenz number is larger than the Sommerfeld value at room temperature and equal to 3.2 × 10^{-8} W·Ω·K^{-2} [115]. Nevertheless, taking into account that the phononic contribution in W is estimated between 1% and 25%, with most of the works in the literature assuming negligible contribution and that the Wiedemann–Franz law still holds for irradiated tungsten [105,116], one can assume that any changes in resistivity due to irradiation will influence the thermal conductivity as well. This means that any recovery of resistivity from annealing in the current study is directly proportional to the recovery of thermal conductivity.

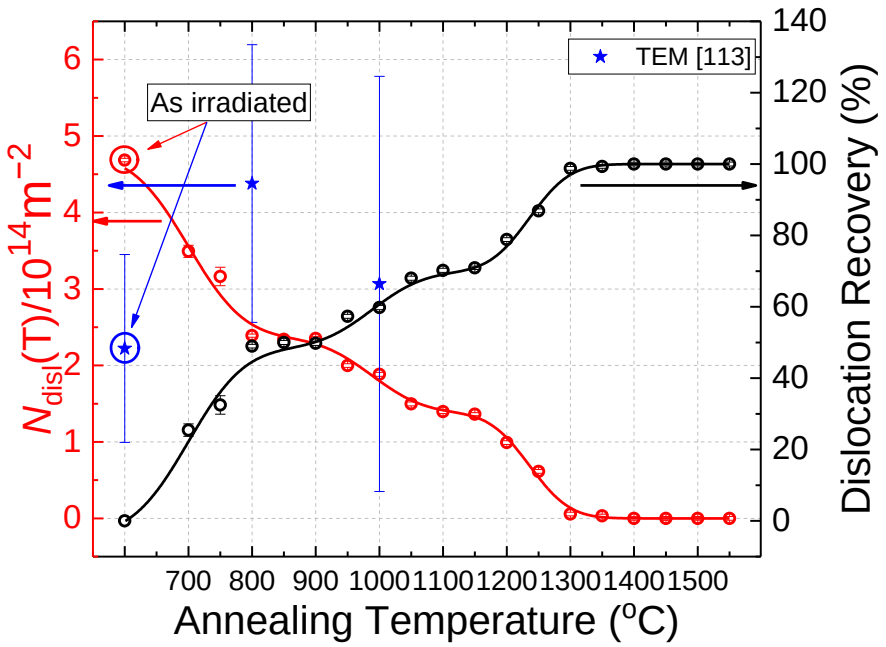

Figure 7. Total dislocation line density (loops and lines) and dislocation recovery percentage for the irradiated sample after post-irradiation annealing determined from the DC electrical resistivity. The TEM-determined total dislocation line density is included for comparison [113]. Solid lines: guides to the eye.

3.4. Crystalline Structure Evolution Versus Annealing (XRD, GIXRD)

XRD and GIXRD measurements were performed after each step of isochronal annealing. XRD patterns of the control and irradiated samples after representative annealing steps are presented in Figure 8.

For the control sample (Figure 8a), signs of recrystallization begin to appear after annealing at 1300 °C, with a significant texture change occurring after annealing at 1350 °C (Figure 8a). This is evidenced by the abrupt increase in the (222) Bragg peak, with the sample reaching an almost monocrystalline (222) texture after annealing at 1400 °C.

Regarding the irradiated sample (Figure 8b), no significant change in the XRD pattern is observed up to 1350 °C. However, after PIA at 1400 °C, a decreasing trend for the (110) Bragg peak can be observed, which may indicate the onset of recrystallization. Comparing this behavior with that of the control sample, it can be inferred that irradiation retards the recrystallization of W while inhibiting abnormal grain growth. This prevents the formation of predominantly (222) grains, which is observed in the control sample.

This effect is more clearly demonstrated in the evolution of the texture coefficient [117] as reported in [71].

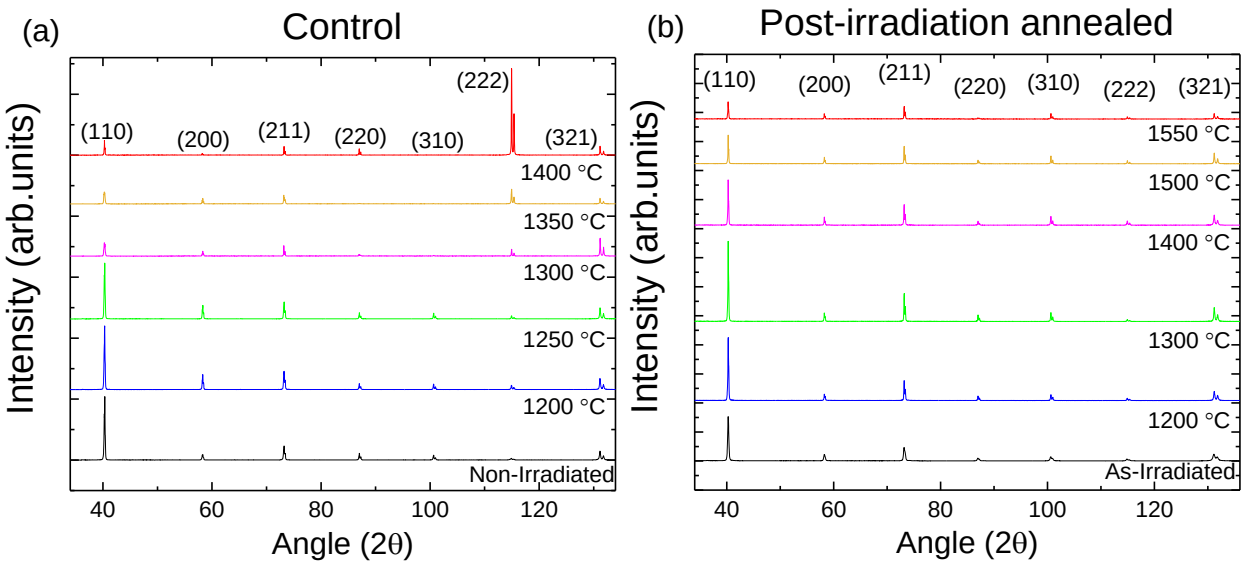

Figure 8. X-ray diffraction patterns after representative steps of annealing (**a**) and post-irradiation annealing (**b**) for the control and irradiated W bar samples, respectively. The (hkl) Miller indices are provided for each Bragg diffraction peak.

The lattice constants, as determined from the position of the W Bragg peaks in the XRD patterns, for the irradiated and control samples after each step of isochronal annealing are presented in Figure 9, along with the lattice constants of the respective electropolished non-irradiated samples.

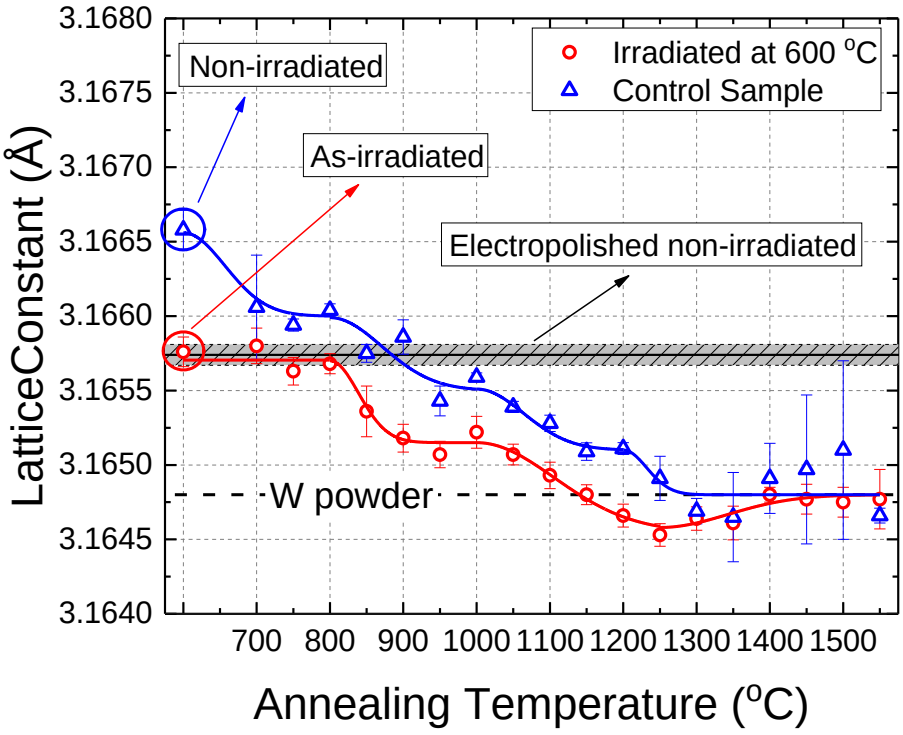

Figure 9. Lattice constants after each step of isochronal annealing for the irradiated and control W samples. The lattice constants of the electropolished W bar and W powder (ICDD PDF:00-0004-0806) are also shown for reference. Lines: guide to the eye.

For the control sample, a decrease in the lattice constant is observed after annealing at 700 °C, which is due to the partial removal of surface stresses caused by the mechanical polishing (Figure 9). Subsequent annealing up to 800 °C does not change the lattice constant, and only after annealing at 850 °C does it attain the value of the electropolished non-irradiated sample. Further annealing up to 1300 °C results in a continuous decrease in the lattice constant. This decrease must originate from the gradual removal of stresses, inherent in the plastically deformed (forged) W material. While the original material is stress relieved at 1000 °C for 1 h, the larger annealing time (24 h) at 950 °C is able to remove some of the stress caused by forging. The lattice constant reaches the unstrained material (W powder) value after annealing at about 1250 °C (Figure 9), which could be indicative of the onset of recrystallization in the material. Further annealing above 1300 °C leaves the lattice constant unchanged within error. It should be noted that the increased uncertainty after annealing at 1350 °C arises from the partial overlapping of multiple Bragg peaks, which affects the accuracy of the Bragg peak position. This is due to the contribution of recrystallized, partially recrystallized, and non-recrystallized parts within the material to the XRD pattern.

The lattice constant of the post-irradiation annealed sample does not change up to annealing at 800 °C. Hence, the first recovery stage present in the control sample is absent in the as-irradiated sample (Figure 9). This indicates that all the surface strain due to the mechanical polishing of the sample prior to the irradiation is removed during the annealing at the irradiation temperature of 600 °C for the duration of 70 days (irradiation time). As the temperature increases above 800 °C, the lattice constant decreases, approaching the value of the unstrained material (W powder, ICDD PDF: 00-0004-0806). After PIA at 1200 °C, it falls below the W powder value (Figure 9), which is attributed to the presence of Re, known to reduce the lattice constant [23]. Specifically, according to [23], the concentration of 0.54 at% Re is expected to decrease the lattice constant by roughly 0.0003 Å, in accordance with the measured difference between the powder value and the lattice constant measured after PIA at 1250 °C. This indicates that the defects affecting the lattice constant are mostly annihilated after PIA at 1250 °C, leaving only the effect of solute Re in the W matrix. After PIA at 1300 °C, the lattice constant seems to recover back to that of the unstrained material, indicating the agglomeration and/or segregation of Re, which reduces its effect on the lattice constant, with an almost complete recovery after PIA at 1450 °C (Figure 9).

By comparing the evolution of the lattice constant between the control and irradiated sample, we observe that, apart from the initial regime at 600 °C that is absent in the irradiated sample, as discussed above, the two following recovery regimes starting at 800 °C and 1000 °C, and concluding near 1250 °C, are shared by both samples. This suggests that these regimes are associated with the release of strain from the annealing of defects which may be either inherent to the material or induced by irradiation, and are also present in the non-irradiated sample. Thus, it is likely that dislocations are the primary defect type responsible for this reduction in strain.

Below, we discuss the values of the Full Width at Half Maximum (FWHM) of the most intense Bragg peak of the XRD patterns ((110) peak), arising only from Cu $K_{\alpha 1}$ irradiation, for the irradiated and control samples after each isochronal annealing. The FWHM is a measure of the micro-strain in the lattice [118], taking into account that the sample crystallite size is large (>1 μm) to influence the evolution of the FWHM. A progressive decrease in the FWHM for both samples with increasing annealing temperature can be observed (Figure 10). This corresponds to a decrease in the dislocation density since dislocations are responsible for causing Bragg peak broadening.

The initial FWHM of the non-irradiated sample reflects the level of deformation caused not only due to the fabrication process but also due to the mechanical polishing.

This is evident from the higher FWHM value compared to that of an electropolished sample. The material attains the FWHM value of the electropolished sample after annealing at 850 °C, which is consistent with the lattice constant evolution of the control sample (Figure 9). After annealing at 900 °C, the FWHM reaches the instrumental resolution value, indicating that almost no defects producing micro-strains remain in the material.

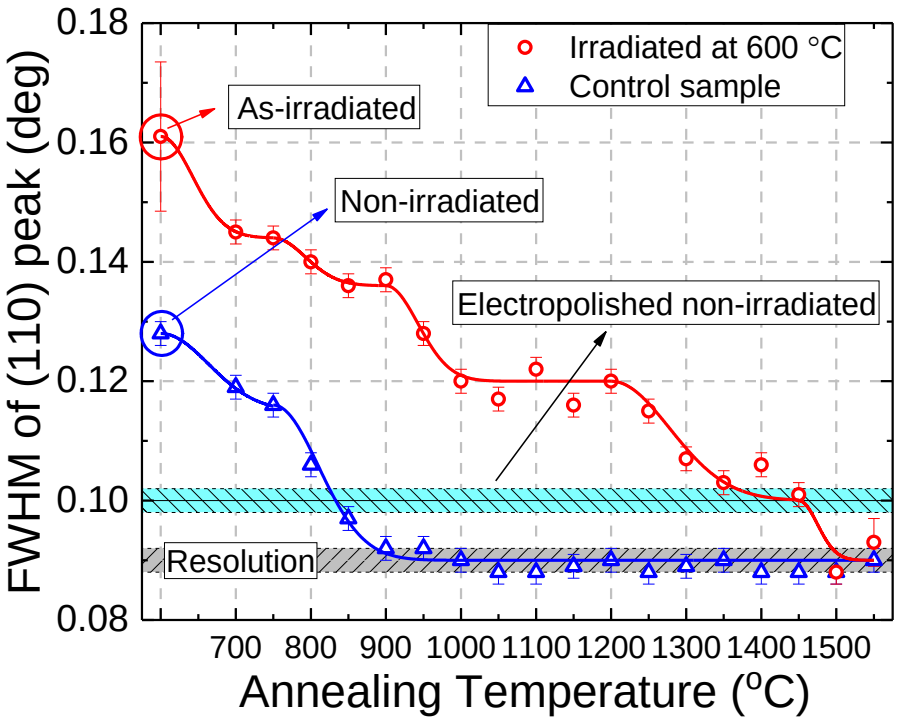

Figure 10. FWHM of the (110) Bragg peak after each step of isochronal annealing for the irradiated and control W samples. The FWHM of the electropolished W bar as well as the instrumental resolution are displayed for comparison. Solid lines: guides to the eye.

For the irradiated material, four recovery regimes can be observed where the FWHM decreases prior to recrystallization at 1500 °C. These recovery stages occur after PIA at 700 °C, at 800 °C, at 950 °C, and at 1250 °C. This suggests that specific dislocation recovery mechanisms are activated at each of these temperatures, as discussed below. Dislocation recovery continues up to 1500 °C, at which point the FWHM attains the resolution value. The irradiated sample reaches the FWHM value of the non-irradiated bar after PIA at 1350 °C. The sharp decrease in the FWHM after PIA at 1500 °C is attributed to recrystallization, bringing the FWHM to the instrumental resolution value, similarly to the behavior observed in the control sample after annealing at 900 °C.

The first two dislocation recovery regimes (600–750 °C and 750–900 °C) are common for both the as-irradiated and the control sample, suggesting partial recovery of the dislocations existing in the sample prior to irradiation. The last two dislocation recovery stages (900–1000 °C and 1200–1450 °C) are only discernible in the irradiated sample, indicating the recovery of dislocations created through irradiation, or more complex dislocation structures that have a higher energy requirement in order to be recovered, such as pinned dislocations from the other irradiation defects existing in the material, for instance, voids or dislocation loops.

Along with the XRD measurements, Grazing Incidence XRD (GIXRD) measurements were performed after each annealing temperature, in order to increase the probed volume and therefore the detection sensitivity of any new phase formation. After PIA at

1550 °C, in addition to the tungsten Bragg peaks, extra peaks were observed (Figure 11). These have been assigned to bcc Re and WOs_2, and sigma phase WRe phases, which are both tetragonal within the $P4_2/mnm$ space group (Figure 11). These additional Bragg peaks have not been detected after annealing below 1550 °C, suggesting a mechanism leading to the local increase in Re and Os concentration, which results in the formation of WRe-σ and WOs_2 phases.

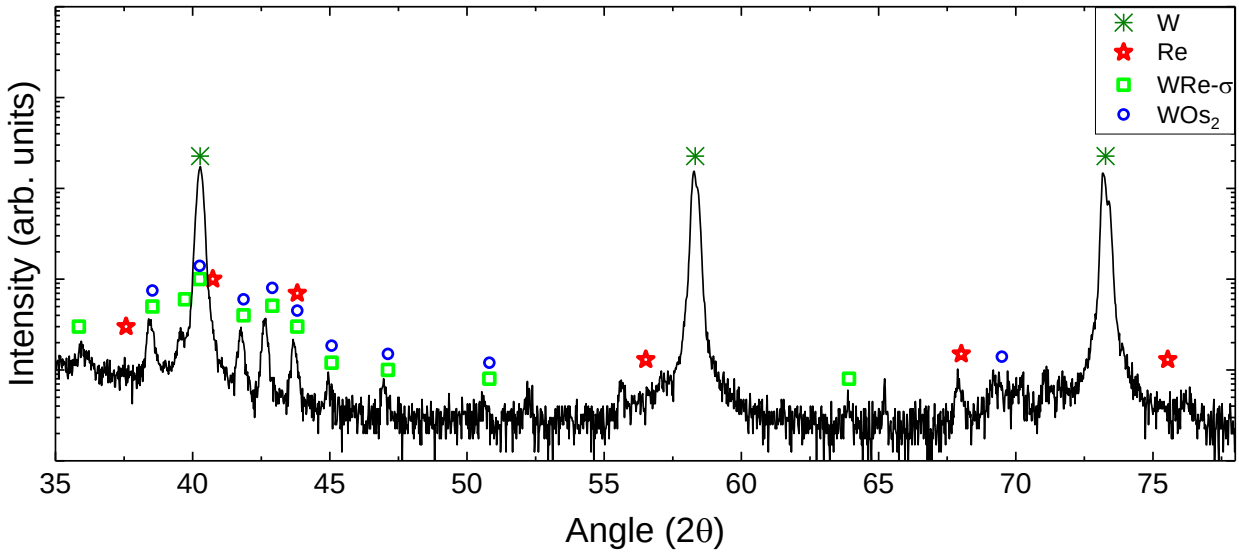

Figure 11. GIXRD pattern of the W sample after PIA at 1550 °C. In addition to W (bcc) peaks, identified phases are Re (bcc), WRe-σ, and WOs_2.

3.5. Vickers Hardness

The determined Vickers hardness after each step of isochronal annealing of both the control and irradiated samples is presented in Figure 12.

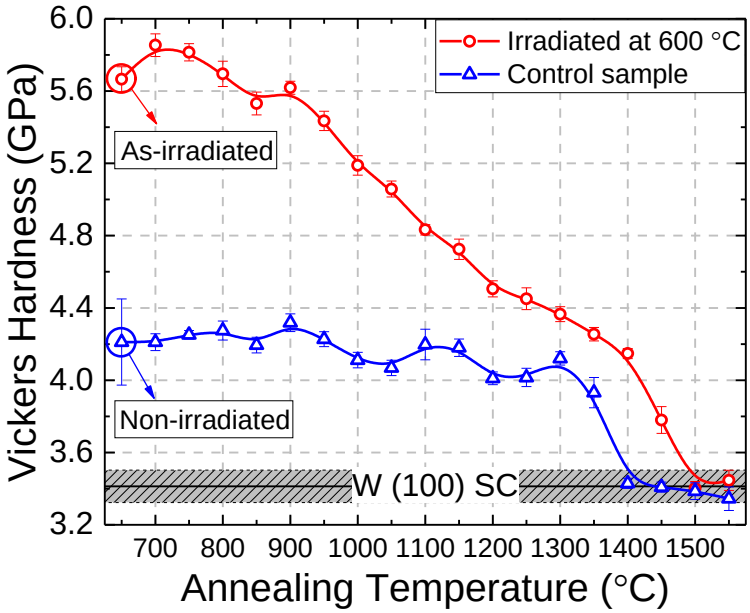

Figure 12. Vickers hardness after each step of isochronal annealing for the W irradiated and control samples. The bar for the non-irradiated reference represents the standard deviation of the meas-

ured values. The Vickers hardness of the W(100) single crystal [37] is shown for comparison. Solid lines: guides to the eye. Adapted from [71].

Regarding the hardness evolution of the control sample, a small decreasing trend can be observed after annealing from 950 °C to 1350 °C. The small fluctuations in hardness reflect dislocation rearrangements as the annealing temperature increases. Finally, after annealing at 1400 °C, the Vickers hardness reaches the value of the non-irradiated W(100) single crystal, indicating that recrystallization and massive grain growth have taken place.

For the irradiated sample, an initial increase in hardness is observed with a peak near 700 °C, followed by a gradual hardness decrease starting after annealing at 900 °C and continuing with higher annealing temperatures. The increase in hardness is probably associated with monovacancy de-trapping and vacancy cluster formation growth. The subsequent decrease beyond 900 °C is attributed to vacancy cluster coarsening and dislocation annihilation. Two distinct recovery regimes are observed: one between 900 and 1200 °C, with a hardness decrease rate of approximately 4 MPa/°C, and a second one from 1200 to 1400 °C, with a reduction rate of about 2 MPa/°C. After PIA at 1350 °C, the hardness of the irradiated sample reaches the value of the non-irradiated reference. Finally, the hardness reduction observed from 1400 to 1500 °C indicates substantial grain growth, with the material exhibiting hardness similar to that of pristine W single crystal after annealing at 1500 °C. This suggests significant grain coarsening and an absence of a significant number of precipitates of transmutation products in the sample.

The radiation-induced hardness, RIH, with respect to the pristine single crystalline W, can be associated with the radiation-induced critical resolved shear stress (CRSS), $\Delta\tau_{CRSS}$, under the assumption that the lattice friction stress remains unchanged with irradiation, by the following relation [119,120]:

$$RIH = k \cdot \Delta\sigma = k \cdot M \cdot \Delta\tau_{CRSS} = k \cdot M \cdot \Delta\tau_{CRSS_{def}} + H_{HP} \quad (9)$$

where $\Delta\sigma$ is the yield strength, k is a factor of 3.2 for tungsten [121], M is the Taylor factor having a value of 3.06 for non-textured BCC and FCC crystals [120], and $\Delta\tau_{CRSS_{def}}$ is the critical resolved shear stress attributed to radiation-induced defects. H_{HP} is the grain boundary hardening, which depends on the grain size according to the Hall–Petch relation [122]:

$$H_{HP} = k_{HP}(T) \cdot d^{-0.5} \quad (10)$$

where k_{HP} is the Hall–Petch coefficient with a value of 3.72 (MPa·m$^{0.5}$) for the W bar grade at room temperature as investigated in [122] and d is the average grain size. The change in hardness above 1300 °C for the control and above 1400 °C for the irradiated sample is attributed to grain growth in agreement with the electrical resistivity results discussed in Section 3.3. The evaluation of the grain size, using Equation (10) and the RIH for the temperature range from 1400 to 1500 °C for the irradiated sample and from 1300 to 1400 °C for the control sample, gives a mean grain size of (26 ± 6) μm and (28 ± 10) μm for the irradiated and control sample, respectively, in fair agreement with the TEM-determined value of 16 μm [24].

Utilizing the dispersed hardening barrier (DHB) model [121,123], the radiation-induced critical resolved shear stress due to defects can be written as:

$$\Delta\tau^2_{CRSS_{def}} = \tau^2_{line} + \tau^2_{loop} + \tau^2_{void} = G^2 b^2 \left(h^2_{line}\rho_{line} + h^2_{loop}\rho_{loop} + h^2_{void}\rho_{void} \right) \quad (11)$$

where G is the shear modulus (159 GPa), b is the Burgers vector (0.274 nm), h_{line} is the dislocation line strength coefficient equal to 0.26 [124], h_{loop} has the value of 0.15 [17], h_{void} is the defect strength of voids, which is dependent on their size [82], and ρ is the obstacle length density ($\rho = N \cdot d$, N the defect number density and d the defect size). Since the strengths of dislocation lines and loops are similar, and the loop density in the irradiated sample is approximately 30 times higher than that of the lines, Equation (11) can be approximated as:

$$\Delta\tau^2_{CRSS_{def}} = G^2b^2\left(h^2_{line}\rho_{line} + h^2_{loop}\rho_{loop} + h^2_{void}\rho_{void}\right) \approx G^2b^2\left(h^2_{loop}\rho_{disl} + h^2_{void}\rho_{void}\right) = \tau^2_{disl} + \tau^2_{void} \quad (12)$$

where $\rho_{disl} = \rho_{loop} + \rho_{line}$. From the total dislocation line density determined by the resistivity (Figure 7), the CRSS arising from all the dislocations (loops and lines), τ_{disl}, can be determined as $\tau_{disl} = Gbh_{loops}\sqrt{\rho_{disl}}$ and is presented in Figure 13. The CRSS arising from voids is also calculated as $\tau_{void} = \sqrt{\Delta\tau^2_{CRSS} - \tau^2_{disl}}$ and is presented in Figure 13, along with the continuous recovery line concerning the CRSS, $\Delta\tau^{calc}_{CRSS} = \sqrt{\left(\tau^{calc}_{disl}\right)^2 + \left(\tau^{calc}_{void}\right)^2}$.

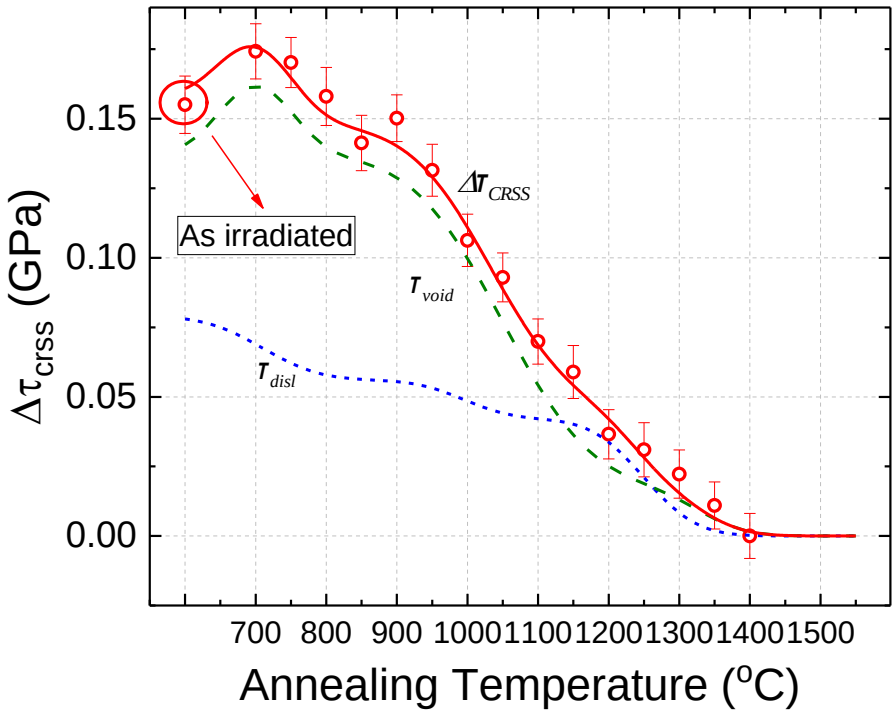

Figure 13. Defect-induced critical resolved shear stress of the post-irradiation annealed sample, calculated from Equations (9), (10), and (12). Dotted line: contribution of dislocations, $\tau_{disl} = Gbh_{loops}\sqrt{\rho_{disl}}$, where ρ_{disl} is obtained from the resistivity measurements (Figure 7). Dashed line: contribution of voids, $\tau_{void} = \sqrt{\Delta\tau_{CRSS}{}^2 - \tau_{disl}{}^2}$. Continuous line: sum of the contribution from dislocations and voids $\Delta\tau^{calc}_{CRSS} = \sqrt{\left(\tau^{calc}_{disl}\right)^2 + \left(\tau^{calc}_{voids}\right)^2}$.

Employing the derived critical resolved shear stress due to the presence of voids, a further quantitative determination of the void sizes and densities can be made by combining the results from PALS and hardness as is presented below.

The obtained lifetime τ_2^{exp} can be connected with the void size by combining the PALS and TEM results [24]. Following the methodology applied in our previous work and using Equation (8) from [37], the average void size was determined as a function of the long positron lifetime, τ_2^{exp}, for annealing temperatures up to 1000 °C.

The determined void size ((1.6 ± 0.2) nm) using the methodology above in the as-irradiated material at 600 °C is in very good agreement with the one determined by TEM ((1.4 ± 0.3) nm) [24].

The number density of voids, N_{void}, can be derived from τ_{void} (Figure 13), as a function of the annealing temperature, using the relation:

$$\tau_{void} = Gbh_{void}\sqrt{\rho_{void}} = Gbh_{void}\sqrt{N_{void}d_{void}} \quad (13)$$

The void obstacle strength, h_{void}, by utilizing the data from [82] depends on the void size as described by the equation:

$$h_{void} = Cd_{void}^{n} \quad (14)$$

where $C = (0.144 \pm 0.024)\,\mathrm{nm}^{-n}$ and $n = 0.56 \pm 0.16$.

The number density of the voids, N_{void}, was determined using Equations (13) and (14), and it is presented in Figure 14. The N_{void} of the as-irradiated sample obtained by this procedure is (16 ± 7) × 10^{22} m^{-3}, which is in fair agreement with the values obtained by TEM ((4.1 ± 1.1) × 10^{22} m^{-3}) taking into account the fact that voids with size ≤1 nm are not resolved by TEM [125]. Above 1000 °C, no data are displayed in Figure 14 due to the saturation of the positron lifetime, which prevents the determination of the void size. However, it can be inferred from Figure 5b that the void density progressively decreases up to 1450 °C. At this temperature, the PALS results indicate that the material has become void free. The continuous line in Figure 14 corresponds to the equation $N_{void}(T) = 16\times10^{22}\cdot exp\left(-\frac{T(^{o}\mathrm{C})-600}{115}\right)\mathrm{m}^{-3}$.

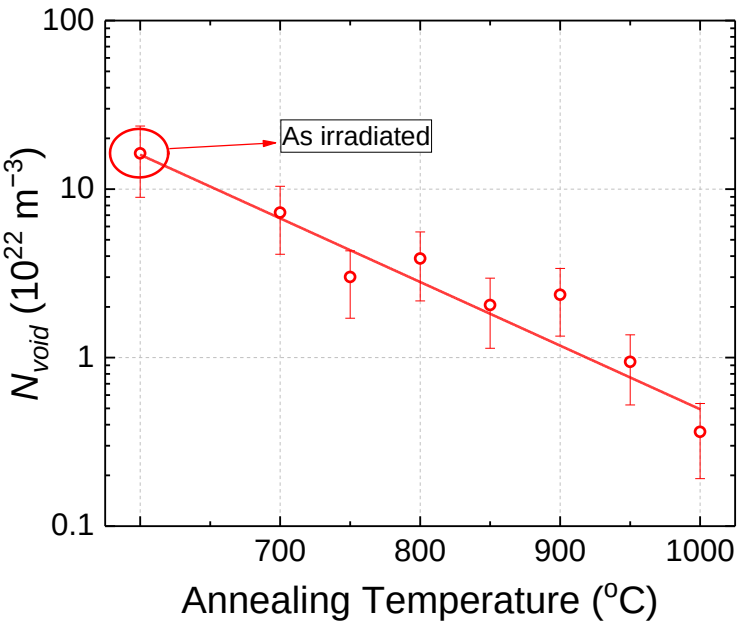

Figure 14. Number density of voids versus annealing temperature for the post-irradiation annealed W bar. Points (O): experimental data, Line: least-square fit (for details see text).

4. Discussion

The investigation of the evolution of the properties of post-irradiation annealed tungsten and of the corresponding microstructural changes causing this evolution, provides a more comprehensive understanding of the evolving microstructure.

The FWHMs of the Bragg peaks, PALS results, electrical resistivity, and hardness are all affected by changes in the dislocation density. The recovery stages concerning dislocation density as derived from resistivity and the FWHM of the (110) Bragg peak and depicted in Figure 7 and Figure 10, respectively, are in general agreement. The first two recovery stages observed in the FWHM (Figure 10), i.e., after PIA at 700 and 800 °C, are smoothed out in the dislocation density determined from resistivity (Figure 7) and appear as an almost continuous stage up to 900 °C. The observed decrease in both the FWHM and resistivity is attributed to dislocation loop growth which continues in the temperature range 900–1150 °C. The resistivity decrease after PIA in the temperature range 1150–1300 °C is probably due to dislocation annihilation, in broad agreement with the FWHM decrease in the range 1200–1450 °C (Figure 10). The evolution of the short positron lifetime (Figure 5), which is associated with dislocations, indicates that dislocation recovery carries on even after the resistivity has been almost completely saturated to its minimum value. This attests to the exceptional sensitivity of PALS. In any case, the temperature at which about less than 5% of the initially neutron irradiation-produced dislocations remain is ~1280 °C.

The evolution of voids or vacancy clusters is more complex, with both void size and density affecting the sample's hardness and resistivity, and the obtained positron lifetimes. Insight can be gained by studying the control sample, where an increase in the mean positron lifetime after annealing at 700 °C (Figure 4) suggests the activation of vacancy de-trapping and migration at that temperature. Similarly, in the irradiated sample, the increase in the lifetime associated with voids (Figure 5a), along with the corresponding increase in hardness originating from voids (Figure 12), indicates the de-trapping and subsequent coalescence of vacancies. This phenomenon may influence the resistivity of the material, contributing to the sudden drop in resistivity after annealing at 700 °C. An Ostwald ripening mechanism of the voids is in effect after annealing in the range of 900–1150 °C. This is inferred by the decrease in hardness (Figure 13), coupled with the void size increase as revealed by the increase in the positron lifetime corresponding to voids (Figure 5a). After annealing at 1250 °C, void dissolution starts (Figure 13), which is also inferred by the drop in the intensity of the positron lifetime corresponding to voids in this temperature range (Figure 5b). Complete void dissolution has occurred after annealing at 1450 °C (Figure 5b), coinciding with a sudden drop in hardness attributed to recrystallization (Figure 12). The temperature at which less than about 5% of the initially neutron irradiation-induced critical resolved shear stress from voids remain is ~1360 °C.

Lastly, the increase in the lattice constant from its minimum value after PIA at 1300 °C (Figure 9) and beyond is indicative of Re depletion from the W matrix, which most probably agglomerates. This Re agglomeration can be inferred from the observation of bcc Re and sigma phase WRe phases in the GIXRD pattern after annealing at 1550 °C. In addition to these phases, WOs_2 is detected. However, these phases have to be in fairly low quantities since the sample maintains the hardness of a pristine W single crystal after annealing at $T \geq 1500$ °C. It is noted that the formation of WRe and WOs_2 phases is not expected according to the phase diagram for the transmutation production that takes place at the investigated dose of 0.21 dpa.

Conclusively, the recovery stages of the irradiated at 0.21 dpa W bar material can be summarized as in Table 3.

Table 3. Recovery stages observed after post-irradiation annealing of W bar.

Mechanism	Temperature (°C)
Vacancy de-trapping and migration	700–750
Dislocation Recovery I—loop growth	700–900, 900–1150
Dislocation Recovery II—loop dissolution	1150–1550
Nearly complete dislocation annihilation	~1280
Increase in void size—Ostwald ripening	900–1150
Void dissolution	1250–1450
Re-segregation and/or agglomeration	1250–1450
Recrystallization	1450
Re/WRe/WOs phase formation	1550

A comparison between the recovery mechanisms and the evolution of the microstructure of the neutron-irradiated bar studied in the current work and the W(100) single crystal studied in [37] is of particular interest. Regarding both dislocation and void recovery, the identification of three recovery mechanisms in the bar is more evident than in the single crystal. It seems that while grain boundaries add more complexity to the microstructure, their presence as defect sinks speeds up the recovery mechanisms once they are activated and allows for their distinction. It has to be noted that dislocation recovery at a rate of 95% occurs approximately 130 °C earlier in the single crystal compared to the bar. However, the trend reverses for the voids, with their complete dissolution occurring ~140 °C earlier in the bar. This again emphasizes the influence of grain boundaries in the material and their complex interactions with different defect types.

5. Summary and Conclusions

A tungsten bar, manufactured by PLANSEE SE via a powder metallurgical process involving sintering and hot forging from two orthogonal directions, was irradiated to 0.21 dpa at 600 °C in the BR2 reactor, at SCK CEN. The microstructure of the as-irradiated sample, as had been previously investigated through TEM [24], showed the existence of vacancy clusters having a size of (1.4 ± 0.3) nm and a density of (4.1 ± 1.1) × 10^{22} m^{-3}. Dislocation loops and lines were also observed, leading to a total linear dislocation density of (2.2 ± 1.2) × 10^{14} m^{-2}. In the current study, post-irradiation annealing was performed under high vacuum, isochronally for 24 h, in the temperature range from 700 to 1550 °C in steps of 50 °C.

The evolution of the microstructure was investigated employing positron annihilation lifetime spectroscopy, X-ray diffraction, resistivity, and Vickers hardness measurements. The combination of the abovementioned techniques allowed for the quantitative determination of the dislocation density after each PIA step, the void size and density up to 1000 °C, and the defect-induced critical resolved shear stress, as well as the identification of the recovery stages as the annealing temperature increases.

Dislocation recovery in the irradiated sample is observed after annealing at 700, 800, and 950, and continuously in the range 1200–1550 °C, as shown by PALS, DC resistivity, and the FWHM obtained from XRD measurements. The first three stages hint towards a loop growth mechanism, enabled through self-climb of the dislocation loops. The last recovery stage (1200–1550 °C) is possibly due to eventual loop annihilation through a vacancy diffusion-aided process.

Regarding the evolution of vacancies and vacancy clusters—voids—as determined from Vickers hardness measurements, this can be split into three stages: 700 °C, 900–1150 °C, and 1250–1450 °C. Vacancy de-trapping and subsequent coalescence towards the formation of vacancy clusters occurs after annealing at 700 °C, followed by an Ost-

wald ripening mechanism starting after PIA at 900 °C and, finally, void dissolution starting after PIA at 1150–1200 °C.

The main transmutation products are Re and Os with the calculated concentrations by FISPACT-II being (0.54 ± 0.06) at% Re and (0.013 ± 0.002) at% Os in solute form. After annealing at 1300 °C, Re segregation is observed, while after annealing at 1550 °C, part of the Re transmutation product has accumulated to larger clusters since the phases of bcc Re and WRe-σ are detected in the GIXRD pattern. Moreover, WOs_2 formation is observed, which indicates the agglomeration of Os in addition to that of Re.

Complete defect recovery occurring at 1450 °C, as inferred from the intensity of the positron lifetime components (Figure 5), coincides with recrystallization at 1450 °C as deduced from the hardness evolution (Figure 12). This suggests that designing a healing process aimed at achieving complete defect recovery without altering the grain structure is challenging. However, annealing at 1300 °C for 24 h could potentially be used to extend the lifetime of fusion reactor components made from this specific W grade. At this temperature, nearly all irradiation-induced dislocations are annihilated and large voids still remain in the microstructure, but their impact on hardness is small, with the material exhibiting a hardness value similar to the non-irradiated state. Furthermore, although Re segregation has started, no detectable precipitates are present. Of course, dose-dependent deviations from this behavior may arise.

Future work could extend the investigation to other tungsten grades, such as cold-rolled grades, or even advanced tungsten materials and alloys. This would not only aid in the selection of optimal tungsten grades for plasma-facing components (PFCs) but also explore the potential of in situ annealing healing processes. Furthermore, conducting coupled isothermal and isochronal annealing on irradiated tungsten materials could eliminate the time-dependent influence on recovery evolution. This approach would enable the determination of activation energies. The activation energies, which are independent of both temperature and time, could serve as a valuable reference for calculations and simulations, essential for future advancements. Additionally, these experiments could provide deeper insights into the fundamental nature of defect interactions.

Author Contributions: Conceptualization, K.M.; Methodology, E.M. and K.M.; Validation, D.P., E.M. and K.M.; Formal analysis, D.P.; Investigation, D.P.; Data curation, D.P.; Writing—original draft, D.P.; Writing—review & editing, E.M. and K.M.; Visualization, D.P.; Supervision, K.M.; Project administration, K.M.; Funding acquisition, K.M. All authors have read and agreed to the published version of the manuscript.

Funding: This work has been carried out within the framework of the EUROfusion Consortium, funded by the European Union via the Euratom Research and Training Programme (Grant Agreement Nos 633053 and 101052200—EUROfusion). The views and opinions expressed are, however, those of the author(s) only and do not necessarily reflect those of the European Union or the European Commission. Neither the European Union nor the European Commission can be held responsible for them. The funding from the Hellenic General Secretariat for Research and Innovation for the Greek National Programme of the Controlled Thermonuclear Fusion is acknowledged.

Data Availability Statement: The original contributions presented in this study are included in the article. Further inquiries can be directed to the corresponding author.

Conflicts of Interest: The authors declare no conflict of interest.

References

1. Pitts, R.A.; Loarte, A.; Wauters, T.; Dubrov, M.; Gribov, Y.; Köchl, F.; Pshenov, A.; Zhang, Y.; Artola, J.; Bonnin, X.; et al. Plasma-wall interaction impact of the ITER re-baseline. *Nucl. Mater. Energy* **2025**, *42*, 101854. https://doi.org/10.1016/j.nme.2024.101854.
2. Bolt, H.; Barabash, V.; Krauss, W.; Linke, J.; Neu, R.; Suzuki, S.; Yoshida, N. Materials for the plasma-facing components of fusion reactors. *J. Nucl. Mater.* **2004**, *329–333*, 66–73. https://doi.org/10.1016/j.jnucmat.2004.04.005.
3. Pitts, R.A.; Carpentier, S.; Escourbiac, F.; Hirai, T.; Komarov, V.; Lisgo, S.; Kukushkin, A.S.; Loarte, A.; Merola, M.; Sashala Naik, A.; et al. A full tungsten divertor for ITER: Physics issues and design status. *J. Nucl. Mater.* **2013**, *438*, S48–S56. https://doi.org/10.1016/j.jnucmat.2013.01.008.
4. Pintsuk, G. Tungsten as a Plasma-Facing Material. In *Comprehensive Nuclear Materials*; Elsevier: Amsterdam, The Netherlands, 2012; Volume 4, pp. 551–581. ISBN 9780080560335.
5. Davis, J..; Barabash, V.; Makhankov, A.; Plöchl, L.; Slattery, K.. Assessment of tungsten for use in the ITER plasma facing components. *J. Nucl. Mater.* **1998**, *258–263*, 308–312. https://doi.org/10.1016/S0022-3115(98)00285-2.
6. Philipps, V. Tungsten as material for plasma-facing components in fusion devices. *J. Nucl. Mater.* **2011**, *415*, S2–S9. https://doi.org/10.1016/J.JNUCMAT.2011.01.110.
7. Yu, J.H.; Tanigawa, H.; Hamaguchi, D.; Nozawa, T. Mechanical properties of three kinds of ITER-Grade pure tungsten with different manufacturing processes. *Fusion Eng. Des.* **2020**, *157*, 111679. https://doi.org/10.1016/j.fusengdes.2020.111679.
8. Reiser, J.; Hoffmann, J.; Jäntsch, U.; Klimenkov, M.; Bonk, S.; Bonnekoh, C.; Rieth, M.; Hoffmann, A.; Mrotzek, T. Ductilisation of tungsten (W): On the shift of the brittle-to-ductile transition (BDT) to lower temperatures through cold rolling. *Int. J. Refract. Met. Hard Mater.* **2016**, *54*, 351–369. https://doi.org/10.1016/J.IJRMHM.2015.09.001.
9. Bonnekoh, C.; Hoffmann, A.; Reiser, J. The brittle-to-ductile transition in cold rolled tungsten: On the decrease of the brittle-to-ductile transition by 600 K to −65 °C. *Int. J. Refract. Met. Hard Mater.* **2018**, *71*, 181–189. https://doi.org/10.1016/j.ijrmhm.2017.11.017.
10. Yin, C.; Terentyev, D.; Pardoen, T.; Bakaeva, A.; Petrov, R.; Antusch, S.; Rieth, M.; Vilémová, M.; Matějíček, J.; Zhang, T. Tensile properties of baseline and advanced tungsten grades for fusion applications. *Int. J. Refract. Met. Hard Mater.* **2018**, *75*, 153–162. https://doi.org/10.1016/j.ijrmhm.2018.04.003.
11. Motojima, O. The ITER project construction status. *Nucl. Fusion* **2015**, *55*, 104023. https://doi.org/10.1088/0029-5515/55/10/104023.
12. Hirai, T.; Panayotis, S.; Barabash, V.; Amzallag, C.; Escourbiac, F.; Durocher, A.; Merola, M.; Linke, J.; Loewenhoff, T.; Pintsuk, G.; et al. Use of tungsten material for the ITER divertor. *Nucl. Mater. Energy* **2016**, *9*, 616–622. https://doi.org/10.1016/j.nme.2016.07.003.
13. Rau, R.C.; Ladd, R.L.; Moteff, J. Voids in irradiated tungsten and molybdenum. *J. Nucl. Mater.* **1969**, *33*, 324–327. https://doi.org/10.1016/0022-3115(69)90029-4.
14. Rieth, M.; Dudarev, S.L.; Gonzalez De Vicente, S.M.; Aktaa, J.; Ahlgren, T.; Antusch, S.; Armstrong, D.E.J.; Balden, M.; Baluc, N.; Barthe, M.F.; et al. Recent progress in research on tungsten materials for nuclear fusion applications in Europe. *J. Nucl. Mater.* **2013**, *432*, 482–500. https://doi.org/10.1016/j.jnucmat.2012.08.018.
15. Buswell, J.T. Vacancy damage in heavy ion and neutron-irradiated tungsten. *Philos. Mag.* **1970**, *22*, 787–802. https://doi.org/10.1080/14786437008220947.
16. Brinkman, J.A. On the Nature of Radiation Damage in Metals. *J. Appl. Phys.* **1954**, *25*, 961–970. https://doi.org/10.1063/1.1721810.
17. Hu, X.; Koyanagi, T.; Fukuda, M.; Katoh, Y.; Snead, L.L.; Wirth, B.D. Defect evolution in single crystalline tungsten following low temperature and low dose neutron irradiation. *J. Nucl. Mater.* **2016**, *470*, 278–289. https://doi.org/10.1016/j.jnucmat.2015.12.040.
18. Ogorodnikova, O.V.; Majerle, M.; Čížek, J.; Simakov, S.; Gann, V.V.; Hruška, P.; Kameník, J.; Pospíšil, J.; Štefánik, M.; Vinš, M. Positron annihilation spectroscopy study of radiation-induced defects in W and Fe irradiated with neutrons with different spectra. *Sci. Rep.* **2020**, *10*, 18898. https://doi.org/10.1038/s41598-020-75737-8.
19. Gilbert, M.R.R.; Sublet, J.-C. Neutron-induced transmutation effects in W and W-alloys in a fusion environment. *Nucl. Fusion* **2011**, *51*, 43005. https://doi.org/10.1088/0029-5515/51/4/043005.
20. Klimenkov, M.; Jäntsch, U.; Rieth, M.; Schneider, H.C.C.; Armstrong, D.E.J.E.J.; Gibson, J.; Roberts, S.G.G. Effect of neutron irradiation on the microstructure of tungsten. *Nucl. Mater. Energy* **2016**, *9*, 480–483. https://doi.org/10.1016/j.nme.2016.09.010.

21. Lloyd, M.J.; Abernethy, R.G.; Gilbert, M.R.; Griffiths, I.; Bagot, P.A.J.; Nguyen-Manh, D.; Moody, M.P.; Armstrong, D.E.J. Decoration of voids with rhenium and osmium transmutation products in neutron irradiated single crystal tungsten. *Scr. Mater.* **2019**, *173*, 96–100. https://doi.org/10.1016/j.scriptamat.2019.07.036.
22. Klimenkov, M.; Dürrschnabel, M.; Jäntsch, U.; Lied, P.; Rieth, M.; Schneider, H.C.; Terentyev, D.; Van Renterghem, W. Microstructural analysis of W irradiated at different temperatures. *J. Nucl. Mater.* **2022**, *572*, 154018. https://doi.org/10.1016/j.jnucmat.2022.154018.
23. Fujitsuka, M.; Tsuchiya, B.; Mutoh, I.; Tanabe, T.; Shikama, T. Effect of neutron irradiation on thermal diffusivity of tungsten–rhenium alloys. *J. Nucl. Mater.* **2000**, *283–287*, 1148–1151. https://doi.org/10.1016/S0022-3115(00)00170-7.
24. Dubinko, A.; Terentyev, D.; Yin, C.; Van Renterghem, W.; Rossaert, B.; Rieth, M.; Zhurkin, E.E.E.; Zinovev, A.; Chang, C.C.C.; Van Dyck, S.; et al. Microstructure and hardening induced by neutron irradiation in single crystal, ITER specification and cold rolled tungsten. *Int. J. Refract. Met. Hard Mater.* **2021**, *98*, 105522. https://doi.org/10.1016/j.ijrmhm.2021.105522.
25. Hu, X. Recent progress in experimental investigation of neutron irradiation response of tungsten. *J. Nucl. Mater.* **2022**, *568*, 153856. https://doi.org/10.1016/j.jnucmat.2022.153856.
26. Hasegawa, A.; Fukuda, M.; Yabuuchi, K.; Nogami, S. Neutron irradiation effects on the microstructural development of tungsten and tungsten alloys. *J. Nucl. Mater.* **2016**, *471*, 175–183. https://doi.org/10.1016/j.jnucmat.2015.10.047.
27. Sikka, V.K.; Moteff, J. Superlattice of voids in neutron-irradiated tungsten. *J. Appl. Phys.* **1972**, *43*, 4942–4944. https://doi.org/10.1063/1.1661050.
28. Fukuda, M.; Yabuuchi, K.; Nogami, S.; Hasegawa, A.; Tanaka, T. Microstructural development of tungsten and tungsten-rhenium alloys due to neutron irradiation in HFIR. *J. Nucl. Mater.* **2014**, *455*, 460–463. https://doi.org/10.1016/j.jnucmat.2014.08.002.
29. Wielunska, B.; Płociński, T.; Schwarz-Selinger, T.; Mayer, M.; Jacob, W.; Ciupiński, L. Dislocation structure of tungsten irradiated by medium to high-mass ions. *Nucl. Fusion* **2022**, *62*, 096003. https://doi.org/10.1088/1741-4326/ac75ff.
30. Dube, C.L.; Kulriya, P.K.; Dutta, D.; Pujari, P.K.; Patil, Y.; Mehta, M.; Patel, P.; Khirwadkar, S.S. Positron annihilation lifetime measurement and X-ray analysis on 120 MeV Au+7 irradiated polycrystalline tungsten. *J. Nucl. Mater.* **2015**, *467*, 406–412. https://doi.org/10.1016/j.jnucmat.2015.05.029.
31. Grzonka, J.; Ciupiński, Ł.; Smalc-Koziorowska, J.; Ogorodnikova, O.V.; Mayer, M.; Kurzydłowski, K.J. Electron microscopy observations of radiation damage in irradiated and annealed tungsten. *Nucl. Instrum. Methods Phys. Res. Sect. B Beam Interact. Mater. Atoms* **2014**, *340*, 27–33. https://doi.org/10.1016/j.nimb.2014.07.043.
32. Yi, X.; Jenkins, M.L.; Kirk, M.A.; Zhou, Z.; Roberts, S.G. In-situ TEM studies of 150 keV W+ ion irradiated W and W-alloys: Damage production and microstructural evolution. *Acta Mater.* **2016**, *112*, 105–120. https://doi.org/10.1016/j.actamat.2016.03.051.
33. Yi, X.; Jenkins, M.L.; Briceno, M.; Roberts, S.G.; Zhou, Z.; Kirk, M.A. In situ study of self-ion irradiation damage in W and W-5Re at 500 °C. *Philos. Mag.* **2013**, *93*, 1715–1738. https://doi.org/10.1080/14786435.2012.754110.
34. Garrison, L.M.M.; Katoh, Y.; Kumar, N.A.P.K.A.P.K. Mechanical properties of single-crystal tungsten irradiated in a mixed spectrum fission reactor. *J. Nucl. Mater.* **2019**, *518*, 208–225. https://doi.org/10.1016/j.jnucmat.2019.02.050.
35. Wang, G.; Li, H.; Li, X.; Li, C.; Li, X.; Xu, R.; Zhu, R.; Li, L.; Zhang, H.; Zhao, Y.; et al. Evolution of low-mode asymmetries introduced by x-ray P2 drive asymmetry during double shell implosions on the SG facility. *Nucl. Fusion* **2024**, *64*, 126002. https://doi.org/10.1088/1741-4326/ad7967.
36. Papadakis, D.; Mergia, K.; Manios, E.; Chatzikos, V.; Dellis, S.; Terentyev, D.; Bonny, G.; Van Renterghem, W.; Chang, C.C.; Messoloras, S. Defect evolution of neutron irradiated ITER grade tungsten after annealing. *Fusion Eng. Des.* **2023**, *189*, 113486. https://doi.org/10.1016/j.fusengdes.2023.113486.
37. Papadakis, D.; Mergia, K.; Manios, E.; Chatzikos, V.; Dellis, S.; Messoloras, S. Post neutron irradiation annealing and defect evolution in single crystal tungsten. *Nucl. Mater. Energy* **2023**, *34*, 101357. https://doi.org/10.1016/j.nme.2022.101357.
38. Lhuillier, P.E.; Barthe, M.F.; Desgardin, P.; Egger, W.; Sperr, P. Positron annihilation studies on the nature and thermal behaviour of irradiation induced defects in tungsten. *Phys. Status Solidi C* **2009**, *6*, 2329–2332. https://doi.org/10.1002/pssc.200982114.
39. Horvath, B.; Dai, Y.; Lee, Y. Annealing effect on the microstructure of tungsten irradiated in SINQ target. *J. Nucl. Mater.* **2018**, *506*, 19–25. https://doi.org/10.1016/J.JNUCMAT.2017.12.020.
40. Nambissan, P.M.G.; Sen, P. Positron annihilation study of the annealing behaviour of alpha induced defects in tungsten. *Radiat. Eff. Defects Solids* **1992**, *124*, 215–221. https://doi.org/10.1080/10420159208220193.

41. Ogorodnikova, V.O.; Dubov, L.Y.; Stepanov, V.S.; Terentyev, D.; Funtikov, V.Y.; Shtotsky, V.Y.; Stolbunov, V.S.S.; Efimov, V.; Gutorov, K.; Ogorodnikova, O.V. V.; et al. Annealing of radiation-induced defects in tungsten: Positron annihilation spectroscopy study. *J. Nucl. Mater.* **2019**, *517*, 148–151. https://doi.org/10.1016/j.jnucmat.2019.02.010.
42. Zibrov, M.; Egger, W.; Heikinheimo, J.; Mayer, M.; Tuomisto, F. Vacancy cluster growth and thermal recovery in hydrogen-irradiated tungsten. *J. Nucl. Mater.* **2020**, *531*, 152017. https://doi.org/10.1016/j.jnucmat.2020.152017.
43. Ogorodnikova, O.V.; Gasparyan, Y.; Efimov, V.; Ciupiński; Grzonka, J. Annealing of radiation-induced damage in tungsten under and after irradiation with 20MeV self-ions. *J. Nucl. Mater.* **2014**, *451*, 379–386. https://doi.org/10.1016/j.jnucmat.2014.04.011.
44. Chauhan, A.; Yuan, Q.; Litvinov, D.; Gaganidze, E.; Schneider, H.C.; Terentyev, D.; Aktaa, J. Effect of temperature on the neutron irradiation-induced cavities in tungsten. *Philos. Mag.* **2022**, *102*, 1665–1683. https://doi.org/10.1080/14786435.2022.2079750.
45. Wang, S.; Guo, W.; Wang, H.; Yi, X.; Ge, L.; Sun, Y.; Cheng, L.; Zhang, X.; Yuan, Y.; Cao, X.; et al. Defect annealing in heavy-ion irradiated tungsten: Long-time thermal evolution of saturated displacement damage at different temperatures. *J. Nucl. Mater.* **2023**, *581*, 154454. https://doi.org/10.1016/j.jnucmat.2023.154454.
46. Breidi, A.; Dudarev, S.L. Dislocation dynamics simulation of thermal annealing of a dislocation loop microstructure. *J. Nucl. Mater.* **2022**, *562*, 153552. https://doi.org/10.1016/j.jnucmat.2022.153552.
47. Zakharova, M.I.; Artemov, N.A.; Bogdanov, V.V. Effects of neutron irradiation and annealing on the elastic moduli and electrical resistivity of molybdenum and tungsten single crystals. *Inorg. Mater.* **2001**, *37*, 786–789. https://doi.org/10.1023/A:1017979230262.
48. Zibrov, M.; Dürbeck, T.; Egger, W.; Mayer, M. High temperature recovery of radiation defects in tungsten and its effect on deuterium retention. *Nucl. Mater. Energy* **2020**, *23*, 100747. https://doi.org/10.1016/j.nme.2020.100747.
49. Burke, J.E.; Turnbull, D. Recrystallization and grain growth. *Prog. Met. Phys.* **1952**, *3*, 220–292. https://doi.org/10.1016/0502-8205(52)90009-9.
50. Pantleon, W. Thermal stability of the microstructure in rolled tungsten for fusion reactors. *Phys. Scr.* **2021**, *96*, 124036. https://doi.org/10.1088/1402-4896/ac2854.
51. Alfonso, A.; Juul Jensen, D.; Luo, G.N.; Pantleon, W. Thermal stability of a highly-deformed warm-rolled tungsten plate in the temperature range 1100–1250 °C. *Fusion Eng. Des.* **2015**, *98–99*, 1924–1928. https://doi.org/10.1016/j.fusengdes.2015.05.043.
52. Ciucani, U.M.; Thum, A.; Devos, C.; Pantleon, W. Recovery and recrystallization kinetics of differently rolled, thin tungsten plates in the temperature range from 1325 °C to 1400 °C. *Nucl. Mater. Energy* **2019**, *20*, 100701. https://doi.org/10.1016/j.nme.2019.100701.
53. Yu, M.; Wang, K.; Zan, X.; Pantleon, W.; Luo, L.; Zhu, X.; Wu, Y. Hardness loss and microstructure evolution of 90% hot-rolled pure tungsten at 1200–1350 °C. *Fusion Eng. Des.* **2017**, *125*, 531–536. https://doi.org/10.1016/j.fusengdes.2017.05.072.
54. Richou, M.; Durif, A.; Lenci, M.; Mondon, M.; Minissale, M.; Gallais, L.; Kermouche, G.; De Temmerman, G. Recrystallization at high temperature of two tungsten materials complying with the ITER specifications. *J. Nucl. Mater.* **2020**, *542*, 152418. https://doi.org/10.1016/j.jnucmat.2020.152418.
55. Ciucani, U.M.; Pantleon, W. Stagnant recrystallization in warm-rolled tungsten in the temperature range from 1150 °C to 1300 °C. *Fusion Eng. Des.* **2019**, *146*, 814–817. https://doi.org/10.1016/j.fusengdes.2019.01.088.
56. Alfonso, A.; Juul Jensen, D.; Luo, G.N.; Pantleon, W. Recrystallization kinetics of warm-rolled tungsten in the temperature range 1150–1350 °C. *J. Nucl. Mater.* **2014**, *455*, 591–594. https://doi.org/10.1016/j.jnucmat.2014.08.037.
57. Levin, Z.S.; Brady, B.G.; Foley, D.C.; Hartwig, K.T. Recrystallization behavior of tungsten processed by equal channel angular extrusion at low homologues temperature: Microstructure, hardness, and texture. *Int. J. Refract. Met. Hard Mater.* **2019**, *83*, 104966. https://doi.org/10.1016/j.ijrmhm.2019.05.012.
58. Tsuchida, K.; Miyazawa, T.; Hasegawa, A.; Nogami, S.; Fukuda, M. Recrystallization behavior of hot-rolled pure tungsten and its alloy plates during high-temperature annealing. *Nucl. Mater. Energy* **2018**, *15*, 158–163. https://doi.org/10.1016/j.nme.2018.04.004.
59. Xia, F.Z.; Wei, H.G.; Wang, M.P.; Zhu, D.H. Investigation of normal recrystallization and abnormal recrystallization in pure tungsten sheet by EBSD. *Int. J. Refract. Met. Hard Mater.* **2015**, *52*, 98–103. https://doi.org/10.1016/j.ijrmhm.2015.05.009.
60. Nogami, S.; Hasegawa, A.; Fukuda, M.; Rieth, M.; Reiser, J.; Pintsuk, G. Mechanical properties of tungsten: Recent research on modified tungsten materials in Japan. *J. Nucl. Mater.* **2021**, *543*, 152506. https://doi.org/10.1016/j.jnucmat.2020.152506.
61. Wang, K.; Zan, X.; Yu, M.; Pantleon, W.; Luo, L.; Zhu, X.; Li, P.; Wu, Y. Effects of thickness reduction on recrystallization process of warm-rolled pure tungsten plates at 1350 °C. *Fusion Eng. Des.* **2017**, *125*, 521–525. https://doi.org/10.1016/j.fusengdes.2017.03.140.

62. Wang, K.; Ren, D.; Zan, X.; Luo, L.; Zhu, X.; Wu, Y. Recrystallization behavior of pure tungsten hot-rolled with high accumulated strain during annealing at 1250 °C–1350 °C. *Mater. Sci. Eng. A* **2021**, *806*, 140828. https://doi.org/10.1016/j.msea.2021.140828.
63. Tanure, L.; Terentyev, D.; Nikolić, V.; Riesch, J.; Verbeken, K. EBSD characterization of pure and K-doped tungsten fibers annealed at different temperatures. *J. Nucl. Mater.* **2020**, *537*, 152201. https://doi.org/10.1016/j.jnucmat.2020.152201.
64. Lied, P.; Bonnekoh, C.; Pantleon, W.; Stricker, M.; Hoffmann, A.; Reiser, J. Comparison of K-doped and pure cold-rolled tungsten sheets: As-rolled condition and recrystallization behaviour after isochronal annealing at different temperatures. *Int. J. Refract. Met. Hard Mater.* **2019**, *85*, 105047. https://doi.org/10.1016/j.ijrmhm.2019.105047.
65. Pintsuk, G.; Antusch, S.; Weingaertner, T.; Wirtz, M. Recrystallization and composition dependent thermal fatigue response of different tungsten grades. *Int. J. Refract. Met. Hard Mater.* **2018**, *72*, 97–103. https://doi.org/10.1016/j.ijrmhm.2017.11.039.
66. Tanure, L.; Bakaeva, A.; Dubinko, A.; Terentyev, D.; Verbeken, K. Effect of annealing on microstructure, texture and hardness of ITER-specification tungsten analyzed by EBSD, vickers micro-hardness and nano-indentation techniques. *J. Nucl. Mater.* **2019**, *524*, 191–199. https://doi.org/10.1016/j.jnucmat.2019.07.005.
67. Wang, K.; Sun, H.; Zan, X.; Ciucani, U.M.; Pantleon, W.; Luo, L.; Wu, Y. Evolution of microstructure and texture of moderately warm-rolled pure tungsten during annealing at 1300 °C. *J. Nucl. Mater.* **2020**, *540*, 152412. https://doi.org/10.1016/j.jnucmat.2020.152412.
68. Reiser, J.; Bonnekoh, C.; Karcher, T.; Pfleging, W.; Weygand, D.; Hoffmann, A. Recrystallisation towards a single texture component in heavily cold rolled tungsten (W) sheets and its impact on micromechanics. *Int. J. Refract. Met. Hard Mater.* **2020**, *86*, 105084. https://doi.org/10.1016/j.ijrmhm.2019.105084.
69. Zhang, X.-X.; Yan, Q.-Z.; Yang, C.-T.; Wang, T.-N.; Xia, M.; Ge, C.-C. Recrystallization temperature of tungsten with different deformation degrees. *Rare Met.* **2016**, *35*, 566–570. https://doi.org/10.1007/s12598-014-0315-2.
70. Ciucani, U.M.; Thum, A.; Devos, C.; Pantleon, W. Isothermal annealing of thin rolled tungsten plates in the temperature range from 1300 °C to 1400 °C. *Nucl. Mater. Energy* **2018**, *15*, 128–134. https://doi.org/10.1016/j.nme.2018.03.009.
71. Papadakis, D.; Mergia, K. The effect of microstructure on recovery and recrystallization after annealing of two neutron irradiated ITER specification tungsten. *Int. J. Refract. Met. Hard Mater.* **2024**, *121*, 106657. https://doi.org/10.1016/j.ijrmhm.2024.106657.
72. Krimpalis, S.; Mergia, K.; Messoloras, S.; Dubinko, A.; Terentyev, D.; Triantou, K.; Reiser, J.; Pintsuk, G. Comparative study of the mechanical properties of different tungsten materials for fusion applications. *Phys. Scr.* **2017**, *T170*, 014068. https://doi.org/10.1088/1402-4896/aa9292.
73. Plansee SE Brochure: Tungsten, 663 DE 02.09 2000, available online: https://www.plansee.com/en/materials/tungsten.html (accessed on 23 July 2019).
74. Sublet, J.C.; Bondarenko, I.P.; Bonny, G.; Conlin, J.L.; Gilbert, M.R.; Greenwood, L.R.; Griffin, P.J.; Helgesson, P.; Iwamoto, Y.; Khryachkov, V.A.; et al. Neutron-induced damage simulations: Beyond defect production cross-section, displacement per atom and iron-based metrics. *Eur. Phys. J. Plus* **2019**, *134*, 350. https://doi.org/10.1140/epjp/i2019-12758-y.
75. Pelowitz, D.; Durkee, J.; Elson, J.; Fensin, M.; Hendricks, J.; James, M.; Johns, R.; Mckinney, G.; Mashnik, S.; Verbeke, J.; et al. MCNPX 2.7.0 Extensions, Los Alamos, NM (United States), 2011. https://doi.org/10.2172/1058045.
76. Norgett, M.J.; Robinson, M.T.; Torrens, I.M. A proposed method of calculating displacement dose rates. *Nucl. Eng. Des.* **1975**, *33*, 50–54. https://doi.org/10.1016/0029-5493(75)90035-7.
77. Breidokaite, S.; Stankunas, G. Neutron Flux in EU DEMO Divertor Cassette Body Using HCPB and WCLL Breeding Blanket Models. *J. Fusion Energy* **2022**, *41*, 14. https://doi.org/10.1007/s10894-022-00327-7.
78. Federici, G.; Biel, W.; Gilbert, M.R.; Kemp, R.; Taylor, N.; Wenninger, R. European DEMO design strategy and consequences for materials. *Nucl. Fusion* **2017**, *57*, 092002. https://doi.org/10.1088/1741-4326/57/9/092002.
79. Chatzikos, V.; Mergia, K.; Bonny, G.; Terentyev, D.; Papadakis, D.; Pavlou, G.E.; Messoloras, S. Positron annihilation spectroscopy investigation of defects in neutron irradiated tungsten materials. *Int. J. Refract. Met. Hard Mater.* **2022**, *105*, 105838. https://doi.org/10.1016/j.ijrmhm.2022.105838.
80. Sublet, J.-C.; Eastwood, J.W.; Morgan, J.G.; Gilbert, M.R.; Fleming, M.; Arter, W. FISPACT-II: An Advanced Simulation System for Activation, Transmutation and Material Modelling. *Nucl. Data Sheets* **2017**, *139*, 77–137. https://doi.org/10.1016/j.nds.2017.01.002.
81. Black, D.R.; Mendenhall, M.H.; Brown, C.M.; Henins, A.; Filliben, J.; Cline, J.P. Certification of Standard Reference Material 660c for powder diffraction. *Powder Diffr.* **2020**, *35*, 17–22. https://doi.org/10.1017/S0885715620000068.

82. Mergia, K.; Chatzikos, V.; Manios, E.; Dellis, S.; Papadakis, D.; Terentyev, D.; Bonny, G.; Dubinko, A.; Stamatelatos, I.E.; Messoloras, S.; et al. Evolution of microstructure in neutron irradiated cold rolled tungsten and its correlation with hardness. *Fusion Eng. Des.* **2021**, *172*, 112784. https://doi.org/10.1016/j.fusengdes.2021.112784.
83. Giebel, D.; Kansy, J. A New Version of LT Program for Positron Lifetime Spectra Analysis. *Mater. Sci. Forum* **2010**, *666*, 138–141. https://doi.org/10.4028/www.scientific.net/MSF.666.138.
84. Giebel, D.; Kansy, J. LT10 Program for Solving Basic Problems Connected with Defect Detection. *Phys. Procedia* **2012**, *35*, 122–127. https://doi.org/10.1016/j.phpro.2012.06.022.
85. Miccoli, I.; Edler, F.; Pfnür, H.; Tegenkamp, C. The 100th anniversary of the four-point probe technique: The role of probe geometries in isotropic and anisotropic systems. *J. Phys. Condens. Matter* **2015**, *27*, 223201. https://doi.org/10.1088/0953-8984/27/22/223201.
86. *ASTM E112-12*; Standard Test Methods for Determining Average Grain Size. ASTM: West Conshohocken, PA, USA, 2024.
87. Bassani, F.; Liedl, G.L.; Wyder, P. *Encyclopedia of Condensed Matter Physics*; Elsevier: Amsterdam, The Netherlands, 2005; ISBN 9780123694010.
88. Hu, Z.; Desgardin, P.; Genevois, C.; Joseph, J.; Décamps, B.; Schäublin, R.; Barthe, M.-F. Effect of purity on the vacancy defects induced in self–irradiated tungsten: A combination of PAS and TEM. *J. Nucl. Mater.* **2021**, *556*, 153175. https://doi.org/10.1016/j.jnucmat.2021.153175.
89. Krsjak, V.; Kuriplach, J.; Shen, T.; Sabelova, V.; Sato, K.; Dai, Y. Helium behavior in ferritic/martensitic steels irradiated in spallation target. *J. Nucl. Mater.* **2015**, *456*, 382–388. https://doi.org/10.1016/j.jnucmat.2014.10.014.
90. Pang, J.; Li, H.; Zhou, K.; Wang, Z. The correlation between dislocations and vacancy defects using positron annihilation spectroscopy. *Plasma Sci. Technol.* **2012**, *14*, 650–655. https://doi.org/10.1088/1009-0630/14/7/19.
91. Yabuuchi, A. Inverse change in positron lifetimes of vacancies in tungsten by binding of interstitial impurity atoms to a vacancy: A first-principles study. *Nucl. Mater. Energy* **2023**, *34*, 101364. https://doi.org/10.1016/j.nme.2023.101364.
92. Yabuuchi, A.; Tanaka, M.; Kinomura, A. Short positron lifetime at vacancies observed in electron-irradiated tungsten: Experiments and first-principles calculations. *J. Nucl. Mater.* **2020**, *542*, 152473. https://doi.org/10.1016/j.jnucmat.2020.152473.
93. Sato, K.; Hirosako, A.; Ishibashi, K.; Miura, Y.; Xu, Q.; Onoue, M.; Fukutoku, Y.; Onitsuka, T.; Hatakeyama, M.; Sunada, S.; et al. Quantitative evaluation of hydrogen atoms trapped at single vacancies in tungsten using positron annihilation lifetime measurements: Experiments and theoretical calculations. *J. Nucl. Mater.* **2017**, *496*, 9–17. https://doi.org/10.1016/j.jnucmat.2017.09.002.
94. Čížek, J. Characterization of lattice defects in metallic materials by positron annihilation spectroscopy: A review. *J. Mater. Sci. Technol.* **2018**, *34*, 577–598. https://doi.org/10.1016/j.jmst.2017.11.050.
95. Papadakis, D.; Dellis, S.; Chatzikos, V.; Manios, E.; Stamatelatos, I.E.; Messoloras, S.; Mergia, K. Neutron irradiation effects in different tungsten microstructures. *Phys. Scr.* **2021**, *96*, 124041. https://doi.org/10.1088/1402-4896/ac1eb2.
96. Eldrup, M.; Singh, B.N. Studies of defects and defect agglomerates by positron annihilation spectroscopy. *J. Nucl. Mater.* **1997**, *251*, 132–138. https://doi.org/10.1016/S0022-3115(97)00221-3.
97. Troev, T.; Popov, E.; Nankov, N.; Yoshiie, T. Model calculation of positron states in tungsten containing hydrogen and helium. *J. Phys. Conf. Ser.* **2010**, *207*, 012033. https://doi.org/10.1088/1742-6596/207/1/012033.
98. Brailsford, A.D.; Bullough, R. The rate theory of swelling due to void growth in irradiated metals. *J. Nucl. Mater.* **1972**, *44*, 121–135. https://doi.org/10.1016/0022-3115(72)90091-8.
99. Dürrschnabel, M.; Klimenkov, M.; Jäntsch, U.; Rieth, M.; Schneider, H.C.; Terentyev, D. New insights into microstructure of neutron-irradiated tungsten. *Sci. Rep.* **2021**, *11*, 7572. https://doi.org/10.1038/s41598-021-86746-6.
100. Brandt, W.; Paulin, R. Positron Diffusion in Solids. *Phys. Rev. B* **1972**, *5*, 2430–2435. https://doi.org/10.1103/PhysRevB.5.2430.
101. Eldeup, M.; Jensen, K.O. Positron Trapping Rates into Cavities in Al : Temperature and Size Effects. *Phys. Status Solidi* **1987**, *102*, 145–152. https://doi.org/10.1002/pssa.2211020114.
102. Nieminen, R.M.; Laakkonen, J. Positron trapping rate into vacancy clusters. *Appl. Phys.* **1979**, *20*, 181–184. https://doi.org/10.1007/BF00885942.
103. Bakonyi, I. *Accounting for the Resistivity Contribution of Grain Boundaries in Metals: Critical Analysis of Reported Experimental and Theoretical Data for Ni and Cu*; Springer: Berlin/Heidelberg, Germany, 2021; Volume 136; ISBN 0123456789.
104. Andrews, P.V. Resistivity due to grain boundaries in pure copper. *Phys. Lett.* **1965**, *19*, 558–560. https://doi.org/10.1016/0031-9163(65)90776-6.
105. Echols, J.R.; Garrison, L.M.; Reid, N.; Parish, C.M.; Hasegawa, A.; Bhattacharya, A.; Zhong, W.; Morrall, D.; Lance, M.; Katoh, Y. Degradation of electrical resistivity of tungsten following shielded neutron irradiation. *Acta Mater.* **2023**, *257*, 119025. https://doi.org/10.1016/j.actamat.2023.119025.

106. Rossiter, P.L. The electrical resistivity of metals and alloys. *Electr. Resist. Met. Alloy.* **1987; pp. 9–10**. https://doi.org/10.1017/cbo9780511600289.
107. Martin, J.W.; Paetsch, R. Electrical resistivity of voids. *J. Phys. F Met. Phys.* **1973**, *3*, 907–917. https://doi.org/10.1088/0305-4608/3/5/005.
108. Martin, J.W. The electrical resistivity due to structural defects. *Philos. Mag.* **1971**, *24*, 555–566. https://doi.org/10.1080/14786437108217029.
109. Martin, J.W. The electrical resistivity of some lattice defects in FCC metals observed in radiation damage experiments. *J. Phys. F Met. Phys.* **1972**, *2*, 842–853. https://doi.org/10.1088/0305-4608/2/5/008.
110. Rasch, K.D.; Siegel, R.W.; Schultz, H. Quenching and recovery investigations of vacancies in tungsten. *Philos. Mag. A Phys. Condens. Matter. Struct. Defects Mech. Prop.* **1980**, *41*, 91–117. https://doi.org/10.1080/01418618008241833.
111. Uray, L.; Tekula-Buxbaum, P. Resistivity contribution of solutes in tungsten. *J. Less Common Met.* **1986**, *123*, 95–100. https://doi.org/10.1016/0022-5088(86)90119-0.
112. Tanno, T.; Hasegawa, A.; Fujiwara, M.; He, J.-C.; Nogami, S.; Satou, M.; Shishido, T.; Abe, K. Precipitation of Solid Transmutation Elements in Irradiated Tungsten Alloys. *Mater. Trans.* **2008**, *49*, 2259–2264. https://doi.org/10.2320/matertrans.MAW200821.
113. Van Renterghem, W.; Bonny, G.; Terentyev, D. TEM investigation of neutron irradiated and post irradiation annealed tungsten materials. *Fusion Eng. Des.* **2022**, *180*, 113170. https://doi.org/10.1016/j.fusengdes.2022.113170.
114. Callister, W.D.; Rethwisch, D.G. *Fundamentals of Materials Science and Engineering: An Integrated Approach*; Wiley: Hoboken, NJ, USA, 2015; Volume 964.
115. Chen, Y.; Ma, J.; Li, W. Understanding the thermal conductivity and Lorenz number in tungsten from first principles. *Phys. Rev. B* **2019**, *99*, 020305. https://doi.org/10.1103/PhysRevB.99.020305.
116. Tolias, P. Analytical expressions for thermophysical properties of solid and liquid tungsten relevant for fusion applications. *Nucl. Mater. Energy* **2017**, *13*, 42–57. https://doi.org/10.1016/j.nme.2017.08.002.
117. Harris, G.B. Quantitative measurement of preferred orientation in rolled uranium bars. *Lond. Edinb. Dublin Philos. Mag. J. Sci.* **1952**, *43*, 113–123. https://doi.org/10.1080/14786440108520972.
118. Birkholz, M. *Thin Film Analysis by X-Ray Scattering*; Wiley: Hoboken, NJ, USA, 2005; ISBN 9783527310524.
119. Tabor, D. The physical meaning of indentation and scratch hardness. *Br. J. Appl. Phys.* **1956**, *7*, 159–166. https://doi.org/10.1088/0508-3443/7/5/301.
120. Stoller, R.E.E.; Zinkle, S.J.J. On the relationship between uniaxial yield strength and resolved shear stress in polycrystalline materials. *J. Nucl. Mater.* **2000**, *283–287*, 349–352. https://doi.org/10.1016/S0022-3115(00)00378-0.
121. Hu, X.; Koyanagi, T.; Fukuda, M.; Kumar, N.A.P.K.; Snead, L.L.; Wirth, B.D.; Katoh, Y. Irradiation hardening of pure tungsten exposed to neutron irradiation. *J. Nucl. Mater.* **2016**, *480*, 235–243. https://doi.org/10.1016/j.jnucmat.2016.08.024.
122. Xiao, X.; Terentyev, D.; Ruiz, A.; Zinovev, A.; Bakaev, A.; Zhurkin, E.E. High temperature nano-indentation of tungsten: Modelling and experimental validation. *Mater. Sci. Eng. A* **2019**, *743*, 106–113. https://doi.org/10.1016/j.msea.2018.11.079.
123. Zinkle, S.J.; Matsukawa, Y. Observation and analysis of defect cluster production and interactions with dislocations. *J. Nucl. Mater.* **2004**, *329–333*, 88–96. https://doi.org/10.1016/j.jnucmat.2004.04.298.
124. Terentyev, D.; Xiao, X.; Dubinko, A.; Bakaeva, A.; Duan, H. Dislocation-mediated strain hardening in tungsten: Thermo-mechanical plasticity theory and experimental validation. *J. Mech. Phys. Solids* **2015**, *85*, 1–15. https://doi.org/10.1016/j.jmps.2015.08.015.
125. Yi, X.; Sand, A.E.; Mason, D.R.; Kirk, M.A.; Roberts, S.G.; Nordlund, K.; Dudarev, S.L. Direct observation of size scaling and elastic interaction between nano-scale defects in collision cascades. *EPL Europhys. Lett.* **2015**, *110*, 36001. https://doi.org/10.1209/0295-5075/110/36001.